Journal of New Technology and Materials
JNTM
Vol. 02, N°02 (2012) 08-12

OEB Univ. Publish. Co.

Identification of the Tensile Properties of hybrid Composite Material by Artificial Neural Network

Vinay Kumar Singh
Associate Professor, Department of Mechanical Engineering, College of Technology, G. B. Pant University of Agriculture & Technology, Pantnagar-263145 (INDIA)
E-mail : vks2319@yahoo.co.in, Mobile No.: 09760825833

Received: 1 March 2012, accepted: 02 April 2012

Abstract:

Composite materials are made from two or more constituent materials with significantly different physical or chemical properties which remain separate and distinct on a macroscopic level within the finished structure. In the present work a silica-styrene-butadiene rubber hybrid composite material is developed with 1 and 2 wt% of nano sized silica particle and 0.25 to 1.5 wt% of styrene-butadiene rubber mixed in resin. Nonlinear relation between mechanical properties and filler material have been obtained. An artificial neural network (ANN) model with one hidden layer and two neurons seems to be approximate for the prediction of mechanical characteristic from the various weight percentage of filler material. Neural networks trained with the back-propagation algorithm are applied to predict the future values of tensile data with different percentage of constitute material. The influencing indicators of constituent percentage of composite material and strain rate are taken into consideration. The design and implementation of a neural network forecasting system is described that has been developed to estimate mechanical properties with different combination of constituent of developed composite material. The performance of the networks is evaluated by comparing them to the experimental data. The comparison shows that neural networks perform the conventional techniques with regard to the prediction quality.

1. Introduction

Composites are made up of individual material referred to as constituent material. There are two categories of constituent materials: matrix and reinforcement. At least one portion of each type is required. The matrix material surrounds and supports the reinforcement materials by maintaining their relative positions. Inorganic particulate filled epoxy matrix composites have been extensively studied during the last two decades due to their increasing applications in coatings, electronic packaging and dental restoratives [1 & 2]. The particles in these composites are generally of micrometer size. Use of nano particles as fillers in epoxy matrix composites is now a day's attracting a great deal of attention from material scientists, technologists and industrialists [3 & 4].

Experimental obtain mechanical properties of composite with varying constituent are have a limitation because it is very difficult to obtain variation of mechanical properties in between the short range of constituent material. An Artificial Neural Network (ANN) is a statistical method which have single statistical model to solve various problems. This method is very useful for non-linear dependencies variables. A suitable ANN architecture has been optimized by evaluating the changes in root mean square error (RMSE) of network output with the number of neurons in the hidden layer. A back propagation refers to the process by which derivatives of network error, with respect to network weights and biases can be computed, has been used in artificial neural network model.

Mathematical model can be used as vary successful statistical tools for research. Model designed for research are typical more complex, and require both a deep understanding of process nature and a lot of hardly available data [5].

In this paper fitting and prediction of measured data is performed using an artificial intelligence method. For this purpose, two-layer neural networks are used.

In the first part of the paper, mechanical properties of developed hybrid composite material containing different percentage of nano sized silica particle and Styrene-butadiene rubber in an epoxy resin matrix is presented. In the second part of the paper, model are designed and implemented of a neural network forecasting system is described that has been developed to estimate mechanical properties with different combination of constituent of developed composite material.

2. Material and Method

Epoxy resin (CY-230) and Hardener (HY-951) is used as a matrix material. Nano sized silica powder (<142 nm) and synthetic rubber procured from M/s DEGUSSA INDIA Pvt. Limited, New Delhi have been used as a filler material. The solution obtained by mixing silica and acrylic rubber in resin is kept in the furnace at a temperature of 90 ± 10 °C for two hours as per the recommendation of [6]. After two hours the whole solution is taken out and allowed to cool to a temperature of 45°C. When a temperature of 45°C has been attained the hardener HY-951 is mixed with 8 wt% (weight percentage) immediately. Due to addition of hardener high viscous solution has been obtained which is again mixed

mechanically by high speed mechanical stirrer. The viscous solution so obtained is poured in to different moulds for sample preparation for tensile testing.

In the present investigation all the tensile tests are conducted as per ISO test procedure. The tests are conducted on 100 kN servo hydraulic UTM machine (model 2008, ADMET make.) different strain rates under displacement mode of control. The different displacement rates are taken as 0.01 mm/min, 0.1 mm/min, 1 mm/min 10 mm/min and 100 mm/min. All tests are conducted at room temperature.

Artificial neural network (ANN) is an intelligent tool with parallel computational capability. With the recent advances in the technology of Artificial Neural Networks (ANN) [7], It is now possible to develop vary successful nonlinear ANN models to examine very difficult process and relationship. It can perform nonlinear mapping in short duration. Once neural network is trained, it provides acceptable recommendations in a short time. Artificial Neural Network is a system that need to be designed at different levels i.e., node, network and training. The developer must go through a period of trial and error in the design decisions before coming up with the satisfactory design.

The error back-propagation process [8] consists of two passes, a forward pass and a backward pass. In the forward pass, an activity pattern is applied to the input nodes of the network and outputs are produced as the actual response of the network. During the forward pass, the synaptic weights of the network are fixed. During the backward pass the synaptic weights are adjusted in accordance with the error-correction rule. Adjustment of synaptic weights moves the actual outputs to the desired outputs. The model of each neuron in this network includes a differentiable non-linearity; a commonly used nonlinearity that satisfies the requirement is a sigmoidal non-linearity defined by the logistic function.

$$y_j = \frac{1}{1+\exp(-v_j)} \tag{1}$$

Where v_j is the induced local field of neuron j and y_j is the output of the neuron.

In this method, the output y_j, of the neurons is compared with the target or desired output d_j. Consequently an error signal

e_j is produced, where $e_j=d_j-y_j$. This error signal is propagated in the backward direction to adjust the synaptic weights of the network. The corrective action is performed in such a way that the network output approaches the desired one in a step-by-step manner by minimizing the sum-square-error cost function defined as

$$E = \tfrac{1}{2}\textstyle\sum_j e_j^2 \tag{2}$$

3. Result and Discussion

In the present investigation single hidden layered neural network is used in the prediction of mechanical properties of the hybrid composite material. The ANN structure used in the present investigation is shown in Fig 1. Back propagation algorithm is used in training. The training of ANN by back propagation involved three stages: the feed forward of the input training pattern, the calculation and back propagation of the associated errors and the adjustment of the weights.

Fig. 1 illustrated the ANN structure with three input layer, one hidden layer and two output layer. Each layer has different number of neurons. In the present case, three, one and two neurons are taken for input, hidden and output layers, respectively. The functional relationship between input and output variables can be established in the hidden layer may cause, over fitting. Because of over fitting, neuron yields large error for the new data even if the error is very small for training data. Also the larger the network, the complexity is more. Trial error method is used in the present case.

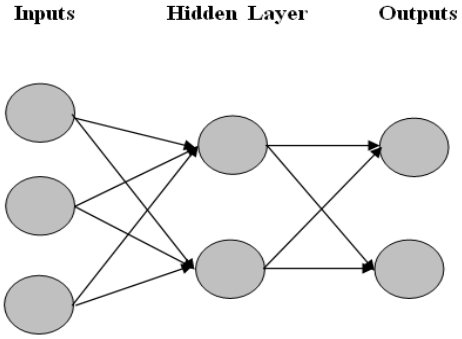

Figure 1. ANN model for tensile strength

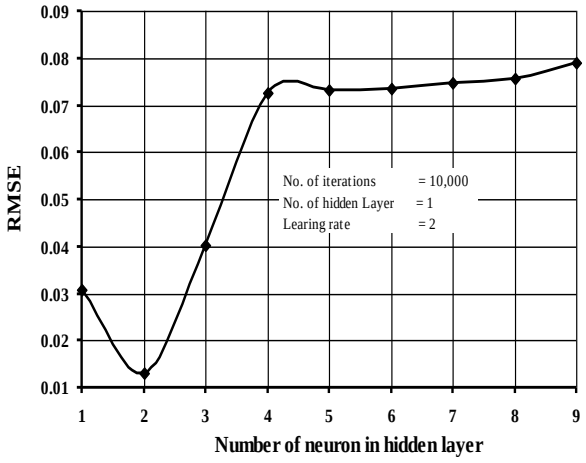

Figure 2. Variation of RMSE value with number of neurons in a hidden layer at 0.1 learning rate

Fig. 2 shows the variation of RMSE with selected neurons at 10,000 iterations. From the Fig. 2, it can be seen that minimum error occurs comparatively to two neurons at the hidden layer. Number of iteration also plays an important role for over fitting. Early stopping or over training may cause higher error and over fitting. Early stopping or over training may also cause higher error and over fitting.

Fig. 3 shows the variation of root mean square error (RMSE) with number of iterations with one hidden layer and two

neurons in hidden layer. Fig. 3, it can be seen that there is no further reduction in RMSE beyond 10,000 iterations. Hence in the present case the ANN structure is trained with 10,000 iterations.

The quality of the prediction also depends on the learning rate parameter, as it influences the RMSE. Higher learning rate parameter indicates an ANN with better output approximation capabilities. In this case also a random technique is applied in the selection of the learning parameter.

The variation of RMSE with learning rate coefficient corresponding to 10000 iterations, one hidden layer and two neurons in hidden layer is shown in Fig. 4. Fig. 4 shows that with learning rate equal to 0.1, high predicatively quality can be achieved with RMSE less 0.0130. As per Universal function approximate theorem, if the less no of neuron is required in the hidden layer for better approximation than only one hidden layer can be used.

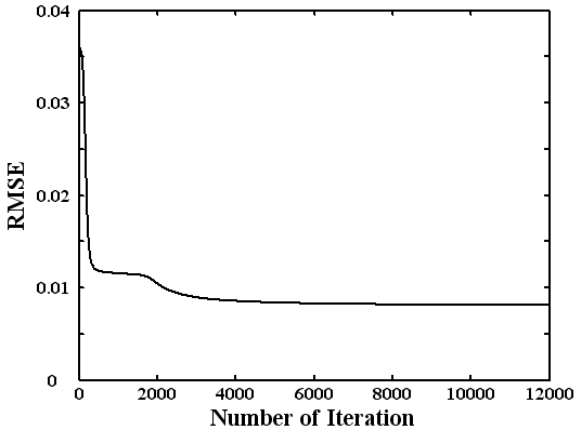

Figure 3. Dependence of RMSE value on Numbers of Iterations at two numbers of neurons in a hidden layer and 0.1 learning rate

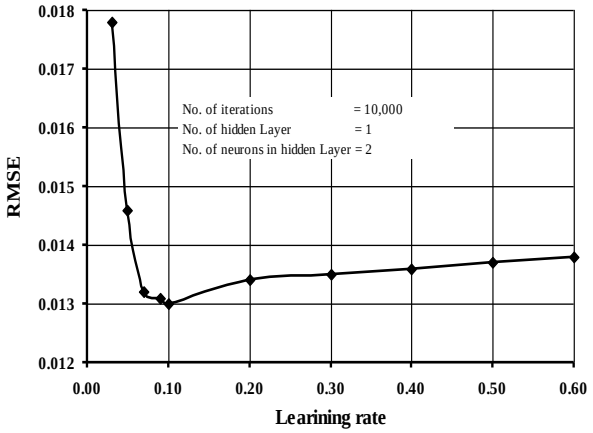

Figure 4. Variation of RMSE value with learning rate at two numbers of neurons in a hidden layer

From the above observations, following ANN configuration is selected to predict the properties of the hybrid composite material.

$$N_{in} - - - - - - - \left[N_{n1}\right]_e - - - - - - - N_{out}$$

Where N_{in} and N_{out} are the element numbers of the inputs and output parameters, respectively and e is the number of neurons in hidden layer. Hence, the optimum ANN architecture is represented as $3-\left[2\right]_1-2$, which means a hidden layer ANN with three input variables and two output variables with a hidden layer containing 2 neurons. The three inputs parameters are rubber (wt %), silica (wt %) and strain rate (mm/min) and two out puts are ultimate tensile strength (σ_u) and modulus of elasticity (E).

Fig. 5-8 shows the training and testing output of the selected ANN structure. Figures indicate that most of the outputs are very close to the experimental data. However, to conclude the effectiveness of the present ANN structure in predicting the ultimate tensile strength and modulus of elasticity, the percentage error between experimental and predicted data is shown in table 1. Table shows that % difference varies from 1.97 to 18.17% for ultimate strength and 9.67 to 18.69% for modulus of elasticity, which are at higher side.

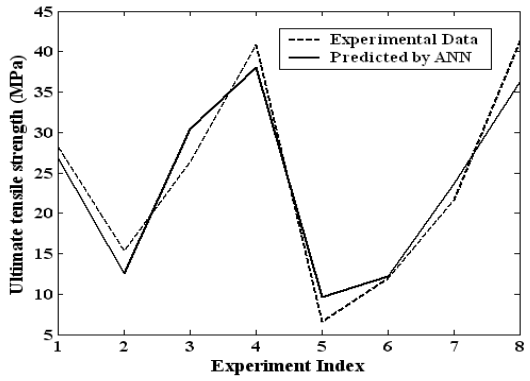

Figure 5. Comparison between Calculated and Target Ultimate Strength for testing data

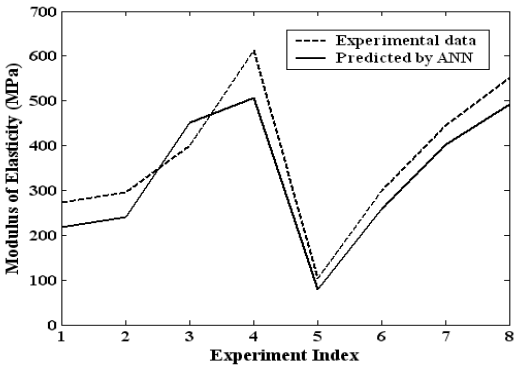

Figure 6. Comparison between Calculated and Target Modulus of Elasticity for testing data

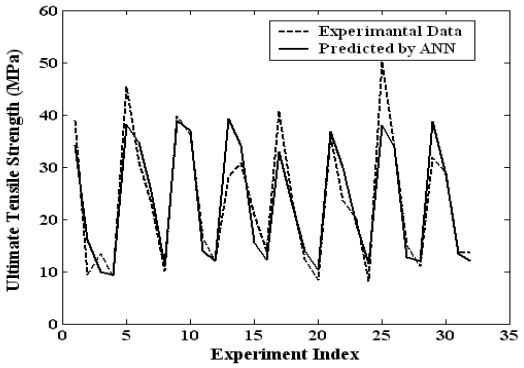

Figure 7. Comparison between Calculated and Target Ultimate Strength for training data

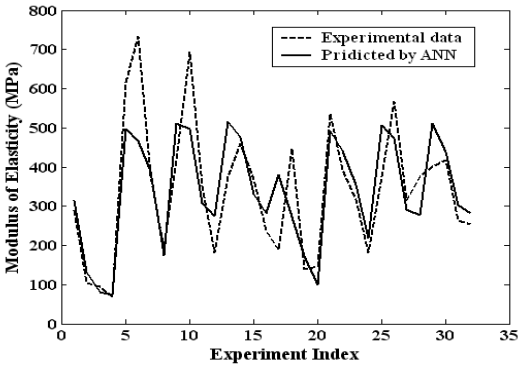

Figure 8.Comparison between Calculated and Target Modulus of Elasticity for training data

Composition at different strain rate			Experimental		Predicted by ANN		% error in ultimate strength	% error in modulus of elasticity
Rubber (wt%)	Silica (wt%)	Strain rate (mm/min)	σ_u (MPa)	E (MPa)	σ_u (MPa)	E (MPa)		
0.25	1.00	0.01	28.16	274.08	26.77	238.39	4.92	13.02
1.00	1.00	0.10	15.33	295.36	12.55	240.15	18.17	18.69
0.50	1.00	1.00	26.40	401.00	30.48	450.65	15.45	12.38
0.25	1.00	10.00	40.79	612.34	38.09	506.30	6.61	17.32
1.50	2.00	0.01	6.60	103.48	7.61	88.21	15.28	14.75
1.00	2.00	0.10	11.98	300.21	12.22	258.56	1.97	13.87
0.50	2.00	1.00	21.70	446.05	23.68	403.02	9.14	9.65
0.25	2.00	10.00	41.30	552.12	36.25	492.46	12.23	10.80

Table 1. Percentage error between experimental and predicted values obtained by ANN

4. Conclusion

ANN requires large number of training data, as it plays a key role in determining ANN predictive quality. As in the present study a very small set of training data is used, the resulted error is at higher side. Hence, a perfect ANN prediction can be achieved by considering enough neurons in the hidden layers. However, too many neurons sufficient measuring data are available. Generation of such large number of experimental data is often very costly. Although, good nonlinear relation between modulus of elasticity and filler material have been obtained.

References

[1] C. A. May, Epoxy Resins-Chemistry and Technology, 2nd ed., Marcel Dekker, New York, USA, (1988).

[2] B. Ellis, Chemistry and Technology of Epoxy Resins, Blackie, London, (1993).

[3] S.K. Bhattacharya and R. R. Tummala, "Integral passives for next generation of electronic packaging: application of epoxy/ceramic nanocomposites as integral capacitors," *Microelectron. J.,* 32 , (2001) 11–19.

[4] M.Z. Rong, M.Q. Zhang, H. Liu, H.M. Zeng, "Microstructure and tribological behavior of polymeric nanocomposites," *Ind. Lubric. Tribol.* 53 (2), (2001)72–77.

[5] K. Johnsen, S. Lisa, R. Teskey, S. Mcnulty and T. Fox, "Process Models as Tools in Forestry Research and Management," *Forest Science*, Vol 47, Number 1, (2001) 2-7.

[6] A. Misra and V. K. Singh, "Experimental Analysis of Two Dimensional Photoelastic Properties Used In

Fracture Mechanics," *Journal of IEI*, Vol. 91, April 18, (2010) 21-24.

[7] S. Haykin, Neural Networks: A compressive Foundation, MaCmillion College publication Company, New Yark.

[8] D.E. Rumelhart, G.E. Hinton and R.J. Williams, "Learning internal representations by error propagation. In McClelland, J.L. & Rumelhart, D.E. (Eds.) Parallel distributed processing," *MA: MIT Press*, Vol. 1. (1986) 318--362 Cambridge.

[9] D. G. Stork and J. D. Allen, "How to solve the N-bit parity problem with two hidden units," *Neural Networks*,Vol.5, (1992)923-926.

Journal of New Technology and Materials
JNTM
Vol. 02, N°02 (2012) 13-17

OEB Univ. Publish. Co.

UV laser irradiation-induced crystallization in titania thick films prepared using a sol-gel method

O. Berkani[a,b], K. Latrous[b], H. El Hamzaoui[c], , M. Bouazaoui[c] and B. Capoen[c]*

[a] *Department of physics, University Mentouri Constantine, Algeria*

[b] *Laboratoire des Composants Actifs et Matériaux,*
Université d'Oum El Bouaghi, 04000 route de Constantine OEB, Algérie

[c] *Laboratoire de Physique des Lasers, Atomes et molécules (PhLAM), UMR 8523*
Université de Lille 1, Sciences et Technologies, 59655 Villeneuve d'Ascq Cedex (France)

* Corresponding author : Tel : +213 6 68 04 72 75; fax: +213 32 47 61 55; Email : w.berkani@univ-oeb.dz

Received: 23 May 2011, accepted: 11 October 2012

Abstract:

Titanium dioxide films of 5 µm thickness have been deposited on soda-lime glass substrates by dip-coating from a suspension of titanium dioxide powder prepared using a sol-gel route. After a heat-treatment, the obtained films have been irradiated using ArF excimer laser. The effect of the laser fluence, ranging between 115 mJ/cm² and 495 mJ/cm²; on the crystallization of the deposited films has been studied. The irradiated areas were characterized using micro-Raman spectroscopy. While the as-deposited films were amorphous, irradiated areas display anatase or rutile crystalline structures, depending on the laser fluence. The corresponding local temperature range was evaluated to 700-800°C. Moreover, the apparent darkening of the layer when increasing the laser fluence was attributed to a re-arrangement of particles under laser-annealing.

Keywords: *Sol-Gel, TiO_2 films, Laser irradiation, Crystallization, Raman spectroscopy.*

1. Introduction

Titanium dioxide (TiO_2) thin films are widely used in various applications such as optical coatings, photovoltaic solar cells, gas sensors, electrochromism, self-cleaning surfaces and catalysis. TiO_2 is also used as a white pigment or as a corrosion-protective coating in ceramics and electrochromic devices [1-5]. Among the three crystallized structures of TiO_2, which are anatase, rutile and brookite, the anatase phase is the most preferred one, due to its excellent photoactivity. However, it is thermodynamically less stable than the rutile phase [6].

During the last years, UV-based methods have been exploited to prepare nc-TiO_2 porous photoanodes for dye-sensitized solar cells. For instance, it can be prepared through the UV-decomposition titania precursor [7]. A high-power irradiation may also be applied to a colloidal titania suspension deposited on plastic substrates for the low-temperature sintering and the elimination of organic additives [8]. A special interest has also been devoted to the crystallization and to the phase transformation of TiO_2 films under different kinds of laser excitation [9-14]. In a recent work, Tebby et al. have successfully obtained nanoporous and nanocrystalline anatase layers on various kinds of substrates through a low-temperature processing of TiO_2 films by UV irradiation for electrochromism applications [15].

On the other hand, for some kinds of applications like photovoltaic cells coatings or gas sensors, it is required to obtain TiO_2 layers of micron-like thickness. Although this objective is difficult to attain by a conventional sol-gel technique [16], thicker layers have been obtained using a technique of titania powder re-dispersion [17].

In this paper, we report on the crystallization of sol-gel derived TiO_2 films induced by ArF excimer laser. Up to 5 µm-thick films could be achieved by using a suspension of sol-gel powder. The crystal phase was studied using micro-Raman spectroscopy. In parallel to these irradiation experiments, TiO_2 powder samples were thermally annealed in order to compare the effect of laser irradiation to that of heat-treatment on the crystallinity of the material.

2. Experimental

2.1 Film deposition

All chemical products have been purchased from Aldrich and used as-received. A TiO_2 sol was prepared using titanium isopropoxide ($Ti(O^iPr)_4$), isopropanol (^iPrOH), and acetic acid (AcOH) with a molar ratio AcOH/Ti=6. The obtained mixture was diluted with methanol. The solution was slowly evaporated at room temperature to yield a powder. Then, the residual solvents (isopropanol, acetic acid and methanol) were eliminated by heating the product at 120°C for 48h. In order to constitute the deposition solution, 3g of the resulting powder was first crushed and then dispersed into 30ml of deionized water containing 125 mg of polyethylene glycol (PEG – MW 35000) used as a dispersal agent. The resulting suspension was kept under stirring for many hours before being used to prepare TiO_2 films.

Soda-lime glass substrates were generally used, except for the sample devoted to thickness measurement by Scanning Electronic Microscopy (SEM). In this latter case, the film was deposited on a cleaved Si wafer. The sol-gel films were

deposited by the dip-coating method using a withdrawal rate of 1 mm/s. Ten consecutive layers were deposited and each layer was dried at 150 °C for 10 min.

2.2 Laser irradiation

After deposition and annealing, the films were irradiated in air for various laser operating conditions using a Lambda Physik ArF excimer laser with a wavelength of 193 nm. The laser fluence per pulse was fixed to a value between 115 mJ/cm^2 and 495 mJ/cm^2, while the number of pulses on the sample was varied from 100 to 800 at a fixed repetition rate of 10 Hz. In this way, the total deposited energy density could be tuned between 11.5 and 396 J/cm^2.

2.3 Characterization

The Raman spectra were obtained in a confocal configuration using a triple-grating spectrometer (Jobin-Yvon T64000) and the 514.5 nm line of an Ar+ laser as the excitation source with a power of 0.2 W. The absence of any phase change under the continuous laser irradiation has been carefully checked prior to the data acquisitions. All Raman spectra were recorded at room temperature in the wavenumber range of 50-700 cm^{-1}. Scanning Electron Microscopy (SEM) images were obtained using a Hitachi TM1000 table-top equipment.

3. Results and Discussion

In order to have an idea of the phase transition temperatures in the TiO_2 products, a dried sol-gel powder was first heat-treated at different temperatures comprised between 350 and 1000°C for 1 hour. In the corresponding Raman spectra of Fig. 1, the most intense Eg vibration band of the anatase phase at 145 cm^{-1} starts to be detected for heat-treatment at 350°C (Fig. 1.a), while the rutile phase begins to be observed at 700°C. Considering that the Raman scattering cross-section is constant for the anatase phase and that the spectra acquisitions have been performed in almost the same conditions, the increasing intensity of each peak in Fig. 1.a may be attributed to the increasing crystallinity of the powder, due to the heat-treatment. Moreover, Fig. 1.b shows the complete and rapid polymorph conversion from anatase to rutile for heat-treatment temperatures between 700 and 800°C.

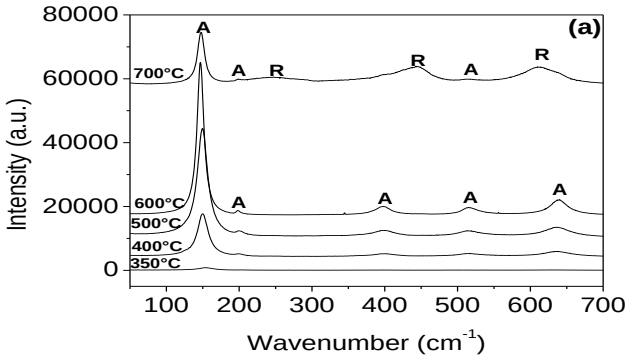

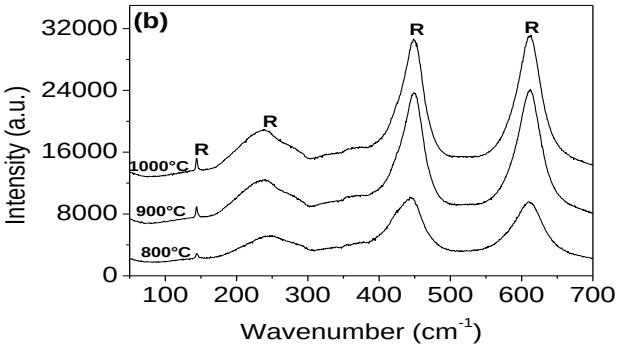

Figure 1. Raman spectra of a TiO_2 powder as a function of annealing temperature (a) 350-700*C, (b) 800-1000°C

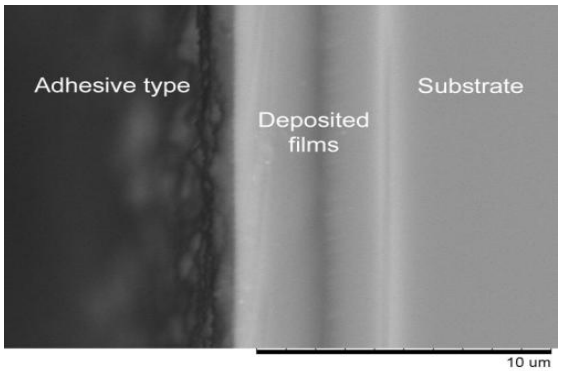

Figure 2. SEM image of the edge of the deposited film on a Si substrate

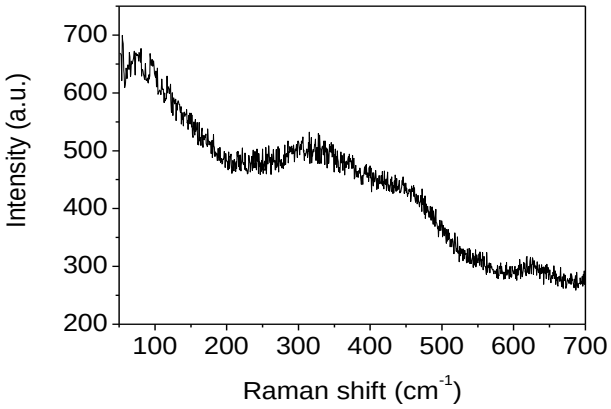

Figure 3. Raman spectra of TiO_2 film dried at 150 °C

Fig. 2 shows a SEM image of the edge of a film deposited on Si substrate and heat-treated at 150°C. The thickness of the film is about 5 µm, which confirms that our preparation route is suitable to obtain a high thickness of the titania film through a sol-gel process.

The TiO_2 film dried at 150°C has an amorphous structure, as revealed in its Raman spectrum (Fig. 3). When such a film is irradiated by the excimer laser beam with average laser fluence per pulse of 115 mJ/cm^2, it remains amorphous, even after a number of pulses as high as 600.

On the contrary, when the pulse fluence is 170 mJ/cm^2, the bands assigned to the six Raman-active fundamental vibrations of the anatase phase could be recorded (Fig. 4.A). Furthermore, as the pulse fluence increases to 495 mJ/cm^2, weaker Raman bands appear (Fig. 4.B), which can be

assigned to the rutile structure of TiO_2. The observed Raman frequencies are listed in Table 1 and compared with previous assignments [12, 16]. This result clearly indicates that the deposited energy is sufficient to generate a local temperature higher than 600°C, making it possible to stabilize the rutile phase.

Table 1. Observed Raman shifts (cm^{-1}) of TiO_2 thin films and their assignment

	This work	H. L. Ma et al. [16]	Toussaint et al. [10]	Assignement
Anatase				
ν_1	145	140.9	144	E_g
ν_2	197	196.3	197	E_g
ν_3	395	396.0	397	B_{1g}
ν_4	514	515.4	518	A_{1g}
ν_5	514	515.4	518	B_{1g}
ν_6	639	632.7	640	E_g
Rutile				
	145	140.2	144	B_{1g}
	239	235.5	230	Multi-phonon process
	437	445.8	448	E_g
	605	609.8	613	A_{1g}

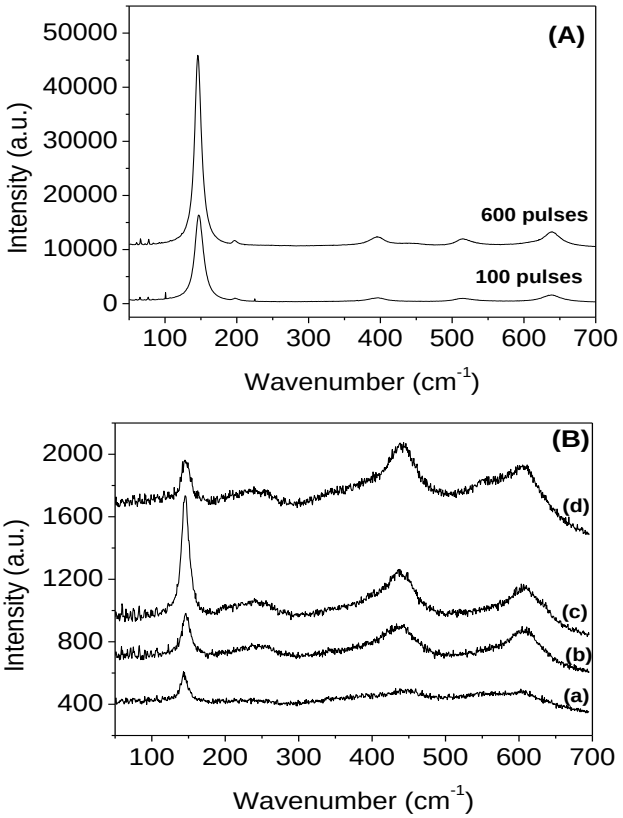

Figure 4. Raman spectra of laser-irradiated TiO_2 films for a pulse fluence of (A) 170 mJ/cm², (B) 495 mJ/cm² with (a) 100 pulses, (b) 400 pulses, (c) 600 pulses, (d) 800 pulses.

Applying a phonon confinement model to the main E_g Raman band of the anatase nanocrystals, it is possible to estimate the crystallite size from the full width at half maximum or from the shift of this peak in comparison to the bulk titania [18]. In the heat-treated powders, the crystal size was found to be (5.5 ± 1.5) nm at a temperature of 350°C, (7.5 ± 1) nm at temperatures ranging between 400°C and 600°C, and (12.5 ± 0.5) nm at a temperature of 700°C. For the laser-irradiated samples, the crystal size was found to be around (12 ± 1) nm for pulse fluence ranging between 115 mJ/cm² and 210 mJ/cm². These energy densities are then supposed to yield a local temperature of about 700°C. No significant change in the crystallite size was observed as long as the crystalline structure remains anatase-like. In the rutile phase, Mazza et al. [19] showed that the E_g peak around 442 cm^{-1} was also submitted to a strong phonon confinement and that the crystal size could be estimated from the peak position or width. Using their correlation curve, the particles mean diameter was found to be around (5± 1) nm in our film irradiated with a pulse fluence of 495 mJ/cm². For comparison, the heat-treated powder exhibit particles with a mean diameter around (4± 0.5) nm at 700°C - 800°C, and around (10 ± 1) nm at 900°C - 1000°C. Hence, it is likely to deduce a local temperature comprised between 700 and 800°C in the laser-treated area, whatever the used fluence. Such a high temperature is believed to completely eliminate the PEG molecules during the laser-sintering process, thus leaving an increased porosity, which would favor the percolation of electrolytes in solar cells electrodes applications [8].

It is worthy to note that the different particles diameters obtained in the two crystal structures produced under similar conditions (i.e. ~ 4 nm for rutile particles and ~ 12 nm for anatase nanocrystals at 700°C) are due to different growth

regimes, the rutile phase being less stable than anatase phase at an intermediate temperature. Furthermore, such a difference also proves that, in the irradiated films, the rutile nanocrystals are note evoluted anatase nanocrystals, but are formed from the beginning of the irradiation, provided that the pulse fluence is sufficiently high.

Another effect of the UV irradiation has been observed when increasing either the pulse fluence or the number of pulses: the apparent color of the irradiated area becomes dark (Fig. 5). This darkening effect has already been reported about PVD-sputtered titania films irradiated using KrF lasers [20]. This effect may be explained by the trapping of light in the surface defects formed during the anatase-to-rutile phase transformation. The coloration phenomenon might also be caused by a partial reduction of titania into TiOx and Ti species under laser irradiation [21]. However, in the case of a titanium sub-oxide, the corresponding transmission spectra of (Fig. 6) should have consisted of a strong and large band peaking around 1000 nm [22].

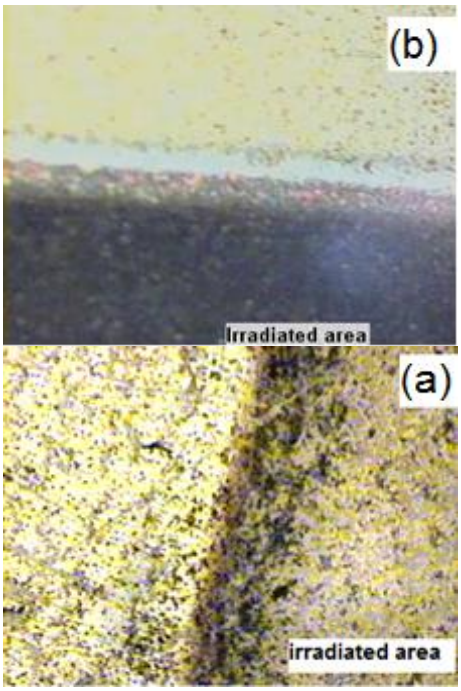

Figure 5. Optical microscopy images of the irradiated area for (a) a laser fluence of 210 mJ/cm², 600 pulses, (b) laser fluence of 495 mJ/cm², 800 pulses.

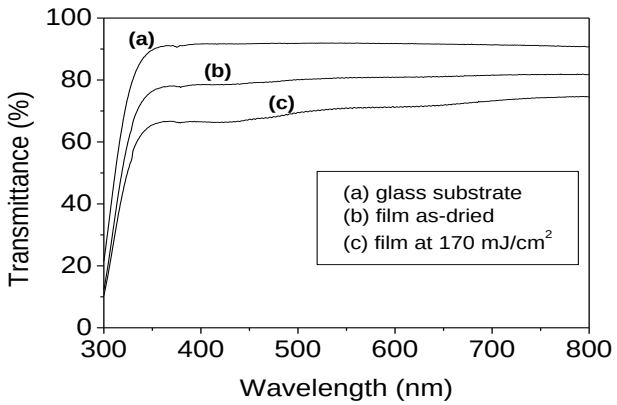

Figure 6. Absorption spectra of (a) the substrate, (b) the as-dried TiO_2 film and (c) the TiO_2 film irradiated at a laser fluence of 170 mJ/cm².

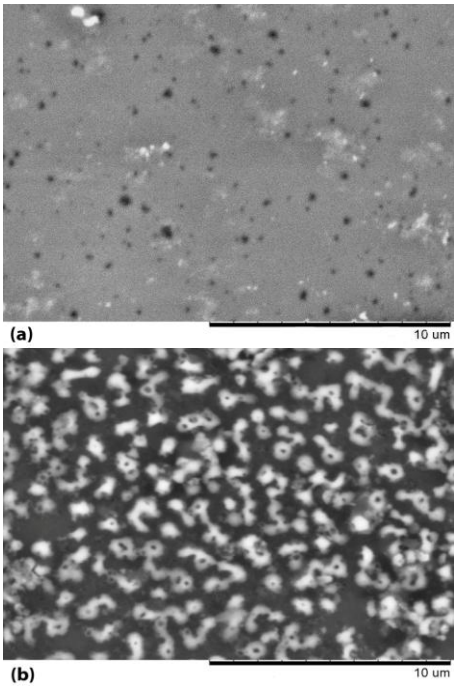

Figure 7. SEM images showing the surface morphology of (a) a non-irradiated area and (b) an area irradiated at a laser fluence of 170 mJ/cm².

Prior to any irradiation, the as-dried film is rather transparent, but as the pulse fluence increases to 170 mJ/cm², the transmittance of an irradiated area decreases, remaining almost flat. Since the whole transmission spectrum decreases, regardless of the wavelength, this phenomenon is probably caused by a scattering or a trapping effect, rather than due to a real absorption. In order to have a better idea of the film evolution under UV-irradiation, the surface morphology was investigated using SEM. As shown in (Fig. 7a), the non-irradiated area consists of a smooth matrix including small particles (diameter less than 1 micron) that can be reasonably designated as the TiO_2 powder particles. On the contrary, the irradiated area presents a rough surface with ring-shaped structures of dimension greater than 1 micron (Fig. 7b). Indeed, the surface heating is sufficient to induce motion of particles in the layer and to re-arrange

them due to surface tension forces. The difference in size and shape of the corresponding light-scattering entities, which have also been observed in PVD films [20], is likely at the origin of the darkening effect. Note that, whatever the physical mechanism occurring in these irradiated films, adjustable optical neutral filters could be manufactured by controlling laser-induced darkening of TiO_2 films so-deposited on glass [21].

4. Conclusion

Crystallization of titanium dioxide films has been performed using ArF excimer laser irradiation and studied as a function of the laser fluence. Anatase phase was achieved at a moderate pulse fluence of 170 mJ/cm^2, while for pulse fluence of 495 mJ/cm^2, the rutile phase was dominant. The crystal size could be derived from the Raman spectra, showing a strong particle size reduction between anatase and rutile structures. This method allows the choice of the selected area of TiO_2 crystallization and the desired crystal phase can be obtained from the adequate choice of laser parameters. Moreover, because it was performed at room temperature, it can be extended to flexible substrates, as organic polymer materials. Furthermore, the apparent darkening of the irradiated TiO_2 was observed, depending on the laser pulse fluence and on the number of pulses. This dependence, which has been explained as a scattering or trapping effect, might be useful for the design of localized adjustable neutral filters.

Acknowledgements

This work has been realized inside at the Centre d'Etudes et de Recherches Lasers et Applications (CERLA), which is supported by the Ministère Chargé de la Recherche, the Région Nord/Pas de Calais and the
Fonds Européens de Développement Economique des Régions.

References

[1] U. Diebold, *Surf. Sci. Rep.* 48 (2003) 53.
[2] S. Meyer, R. Gorges, G. Kreisel, *Thin Solid Films* 450 (2004) 276.
[3] C. Garapon, C. Champeaux, J. Mugnier, G. Panczer, P. Marchet, A. Catherinot, B. Jacquier, *Appl. Surf. Sci.* 96-98 (1996) 836.
[4] T. Yuji, H. Akatsuka, N. Mungkung, B.W. Park, Y.M. Sung, *Vacuum* 83 (2008) 124.
[5] C. Wang, S. Lin, Y. Chen, *J. Phys. Chem. Solid* 69 (2008) 451.
[6] Y. Choi, S. Yamamoto, T. Umebayashi, M. Yoshikawa, *Solid State Ionics* 172 (2004) 105.
[7] D. Gutiérrez-Tauste, I. Zumeta, E. Vigil, M.A. Hernández-Fenollosa, X. Domènech and J. A. Ayllón, *J. Photochem. Photobiol. A: Chem.* 175 (2005) 165.
[8] H. Kim, R.C.Y. Auyeung, M. Ollinger, G.P. Kushto, Z.H. Kafafi and A. Piqué, *Appl. Phys. A* 83 (2006) 73.
[9] N. Asakuma, T. Fukui, M. Aizawa, M. Toki, H. Imai and H. Hirashima, *J. of Sol-Gel Sci. Technol.* 19 (2000) 333.
[10] Y. Wu, K. Choy, L. L. Hench, *Appl. Surf. Sci.* 247 (2005) 378.
[11] O. Van Overschelde, R. Snyders, M. Wautelet, *Appl. Sur. Sci.* 254 (2007) 971.
[12] D. R. Toussaint, L. D. Laude, V. M. Geskin, R. Lazzaroni and R. Gouttebaron, *Thin solid films* 440 (2003) 268.
[13] F. J. Yasir, L. Zhu, *Scripta Mater.* 60 (2009) 467.
[14] H. Ma, G. Guo, J. Yang, Y. Guo, Ninghua Ma, *Nucl. Instr. Meth.* B 264 (2007) 61.
[15] Z. Tebby, O. Babot, T. Toupance, D. Park, G. Campet, and M. Delville, *Chem. Mater.* 20 (2008) 7260.
[16] N. Ozer, H. Demiryont, J. H. Simmons, *Appl. Opt.* 30 (1991) 3661.
[17] E. Traversa, M. L. Di Vona, S. Licoccia, *J. Sol-Gel Sci. & Technol.* 19 (2000) 193.
[18] S. Balaji, Y. Djaoued, J. Robichaud, *J. Raman Spectrosc.* 37 (2006) 1416.
[19] T. Mazza, E. Barborini, P. Piseri and P. Milani, *Phys. Rev. B* 75 (2007) 045416.
[20] H.Y. Zheng, H.X. Qian and W. Zhou, Appl. *Surf. Sci.* 254 (2008) 2174.
[21] H.Y. Zheng, A. Soutar, G.C. Lim, J.W. Chai, B. Freeman and H.J. Jiang, *Appl. Surf. Sci.* 222 (2004) 110.
[22] J. Yao, J. Shao, H. He, Z. Fan, *Vacuum* 81 (2007) 1023.

Journal of New Technology and Materials
JNTM
Vol. 02, N°02 (2012) 18-21

OEB Univ. Publish. Co.

Morphological and physico-chemical characterization of Mn-Bi system electrodeposited in a mixed sulfate-nitrate bath

S. Boudinar, N. Benbrahim, B. Benfedda and A. Kadri
Laboratoire de Physique et Chimie des Matériaux (LPCM), Faculté des sciences, Université Mouloud MAMMERI de Tizi-Ouzou
BP 17 RP Tizi-Ouzou 15000,Algeria

Received: 3 March 2012, revised: 05 July 2012, accepted: 17 October 2012

Abstract:
In this paper, the electrodeposition kinetics of the Mn-Bi system in a mixed sulfate nitrate bath is reported. The plating bath is characterized by the presence of some additives like the boric acid and the ammonium sulfate.
In this work, cyclic voltammetry is used to characterize reduction and dissolution potential of each element. The morphological and the chemical composition of the deposit were determined by scanning electron microscopy (SEM) and energy dispersive spectroscopy (EDS).
The deposit has a heterogeneous appearance with different grain size, the energy dispersive spectroscopy (EDS) analysis reveals the presence of manganese and bismuth peaks with almost the same intensities.
Keywords: *Mn-Bi, Electrodeposition, Cyclic voltammety, SEM, EDS.*

1. Introduction

The development of new magnetic thin films based on transition metals CoPt, FePt [1] and MnBi [2, 3, 4], has attracted considerable attention because of their application in the recording media. Therefore, several works related to the MnBi alloy are reported in the literature; this system is known as a hard magnetic material with a strong magnetic anisotropy along the *c* axis in its hexagonal phase at low temperature. Many workers have investigated the elaboration of the MnBi system using the physical methods, such as molecular beam epitaxial (MBE) [5, 6] and vacuum evaporation [7, 8].
Several baths was reported in the literature to electrodeposition of Mn and Bi separately: sulfate bath [9], chloride bath [10] and nitrate bath [11] with and without additive. But , in our knowledge, there is just one paper related to the electrodeposition of the two element Mn and Bi simultaneously in a chloride bath containing ammonium chloride as an additive[12].

The problem encountered is first of all to find a suitable electrolytic bath for electrodepositing simultaneously the two elements which are characterized by their difference of solubility.
The other problem is related to the very low equilibrium potential value of the Mn^{2+}/Mn couple in aqueous solution ($E_{Mn^{2+}/Mn}$= -1.18V/SHE) compared to that of Bi^{3+}/Bi ($E_{Bi^{3+}/Bi}$= 0.3 V/SHE). In fact reduction of Mn^{2+} to Mn is always accompanied by hydrogen evolution which induces a very low current efficiencies and makes the electrodeposition of Mn alloys in aqueous solution very complicated as it is not easy to control the electrodeposition process [13].The manganese deposit is also easily oxidized [14].

In this work, we propose to study the electrodeposition kinetic of the Mn-Bi system from a mixed sulfate-nitrate bath and the role of the ammonium sulfate as an additive in the electroplating bath.

2. Experimental

Electrochemical experiments were realized in a classical three-electrode glass cell. The working electrode was a vitreous carbon rotating disk electrode (RDE) with an area of 0.2 cm^2. The counter electrode was a platinum wire immersed in a separate compartment containing solution without electroactive metallic cations. Saturated calomel electrode (SCE), mounted in a separate compartment containing solution without electroactive metallic cations was used as reference electrode.
All electrochemical experiments were carried out with an EG &G 273A potentiostat/galvanostat controlled with Power-suite software. The electrolytic baths were composed of 0.4 M $MnSO_4$ $1H_2O$, 10^{-3} M Bi $(NO_3)_3$ $5H_2O$, 0.5 M H_3BO_3 and 1 M $(NH_4)_2SO_4$.
The pH was adjusted to 2 by addition of H_2SO_4. Before the experiments, solutions were deaerated with nitrogen for 15 min. Deposition was realized at room temperature.

3. Results and discussions

3.1 Electrochemical characterization

3.1.1 Cyclic voltammetry of Manganese electrodeposition

Cyclic voltammetry was used to determine the potential region for the deposition and dissolution of bismuth, manganese and manganese-bismuth system. Fig1 (a and b) shows the cyclic voltammogram of Mn deposition and dissolution in a solution containing 0.4 M $MnSO_4$, 0.5 M

H_3BO_3,0 M and 1 M $(NH_4)_2SO_4$ respectively on vitreous carbon electrode at different cathodic limit potential.

For the solution without ammonium sulfate, when the potential sweep in the cathodic direction, starting from the rest potential, no significant current density
was observed until a potential of -1.65V.vs.SCE where the courant density increase rapidly, this is attributed to the proton discharge reaction and may be to the manganese reduction. In the reverse scan no dissolution peak, which could be related to Mn dissolution, is observed. In the case of the solution containing 1M of ammonium sulfate, a significant increase in the current density, with values clearly higher than in the fig1(a), is also observed at -1.65V.vs.SCE, this is attributed to the both hydrogen evolution and manganese reduction with a better current efficiency.

In the reverse scan, a dissolution peak related to the manganese deposit is observed at -1.4 V.vs.SCE. Its intensity increases with increasing the cathodic limit potential. At more cathodic limit potential fluctuations are observed on the voltammograms, these are related to hydrogen evolution.

The presence of the ammonium sulfate additive in the Mn plating bath plays an important role in the improvement of the bath efficiency, indeed in the bath without ammonium sulfate, the hydrogen reduction is so important that it could prevent manganese deposition, this why no dissolution peak is observed in this bath.

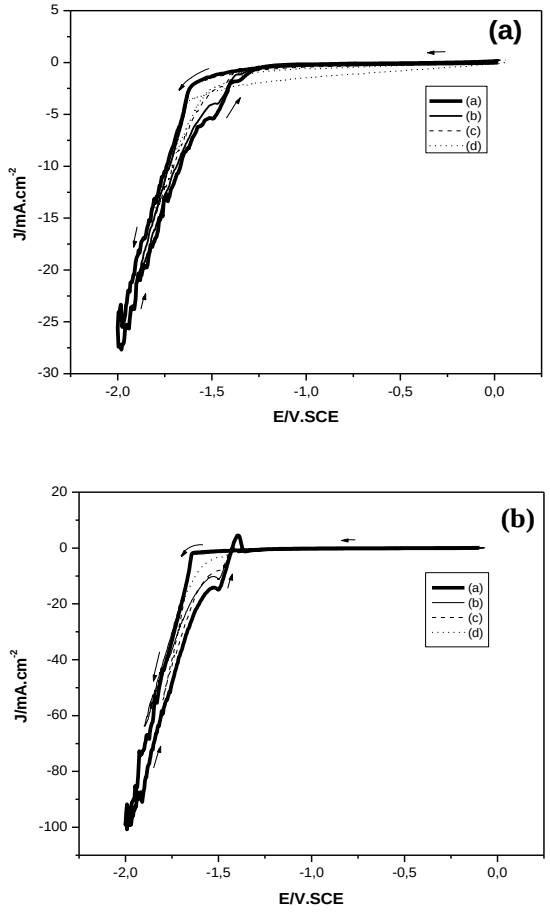

Figure 1. Cyclic voltammety study of Mn deposition, (a) E=-2V.vs.SCE, (b) E=-1.9V.vs.SCE, (c) E=-1.8V.vs.SCE, (d) E=-1.7V.vs.SCE. Vb=20mV.S^{-1}, ω=250rpm. (a) without ammonium sulfate, (b) with 1M of ammonium sulfate.

3.1.2 Cyclic voltammetry of Bismuth electrodeposition

Fig 2 (a, b) shows the cyclic voltammogram of Bi reduction and dissolution on vitreous carbon electrode at different cathodic limit potential in a nitrate bath containing 10^{-3} M $Bi(NO_3)_3$, 0.5 M H_3BO_3,1M $(NH_4)_2SO_4$.

Starting from the rest potential (E= 0.21V.vs.SCE) and sweeping towards the cathodic potential, a plateau of a week current is observed from -0.06V.vs.SCE , it is attributed to the discharge of the first germs of bismuth on the vitreous carbon electrode.

Another reduction wave is clearly observed at -0.15 V.vs.SCE, as we can see on the fig 2(a), the corresponding current density is constant up to -0.3V.vs. SCE, it is the limiting current region where Bi (III) reduction is under mass transport control. Then the current density increase rapidly at -0.6 V.vs.SCE which corresponds to both bismuth reduction and proton discharge reaction.

In the reverse scan, the dissolution peak of Bi is observed at 0.009 V.vs.SCE. Its intensity increases with the cathodic limit potential; this can be explained by the increase of the Bi deposits during the cathodic scan fig 2(b).

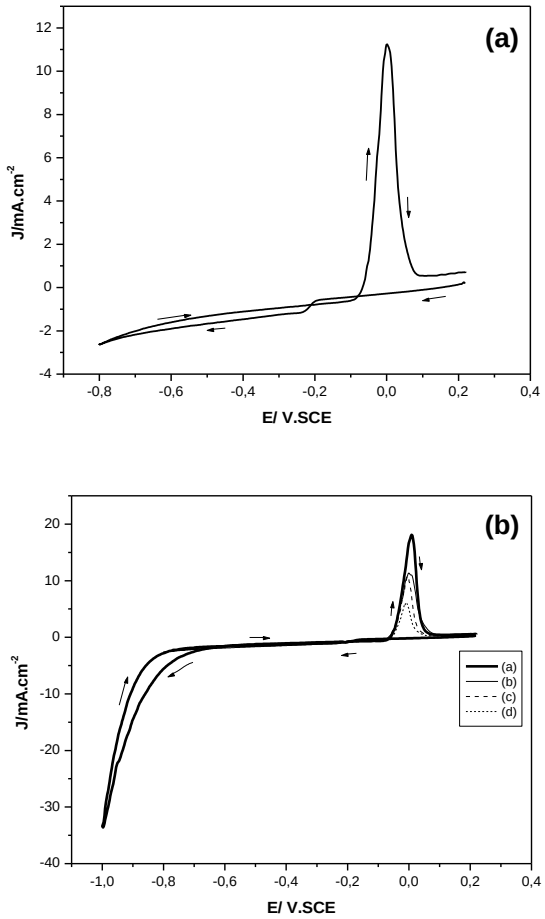

Figure 2. Cyclic voltammetry study of Bi deposition (a) E=-0.8V.vs.SCE, (b) at different cathodic limit potential (a) E=-1V.vs.SCE, (b) E=-0.8V.vs.SCE, (c) E=-0.6V.vs.SCE, (d) E=-0.4V.vs.SCE. Vb=20mV.S^{-1}, ω =250rpm.

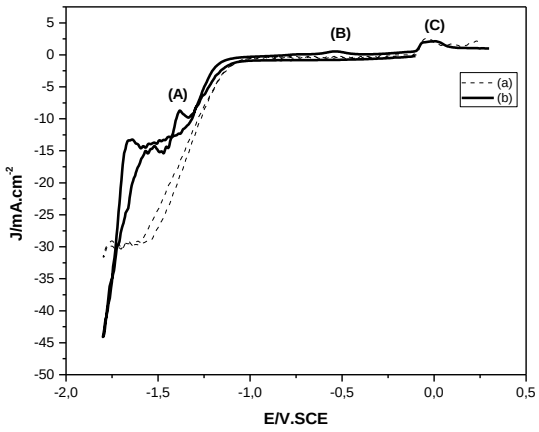

Figure 3. Cyclic voltammetry study of Mn-Bi co deposition. (a) without ammoniun sulfate , (b) with 1M of ammonium sulfate.Vb= 20mV.S^{-1}, ω=250rpm.

3.1.3 Cyclic voltammetry of Mn and Bi co-deposition

To study the electrodeposition kinetics of the Mn-Bi system in a mixed sulfate-nitrate bath containing both Mn^{2+} and Bi^{3+} ions, some problems related to the difference of the two ions solubility has been encountered. Consequently a study of electrochemical kinetics of Mn-Bi as a function of the pH is necessary to avoid Mn and Bi precipitation. From this study it was found that the pH value of 2 is required to avoid this precipitation.

Fig.3. shows the cyclic voltammogram of Mn-Bi deposition and dissolution on vitreous carbon electrode in presence and absence of ammonium sulfate. The cathodic limit potential was fixed at -1.8 V.vs.SCE and the pH was adjusted to 2.

In the voltammogram without the ammonium sulfate, starting from the rest potential (E=-0.11V.vs.SCE) and scanning towards the cathodic potential, a weak current plateau corresponding to the discharge of bismuth on the vitreous carbon electrode is observed. A significant increase in the current density is observed at -1V.vs.SCE, this correspond to the hydrogen evolution at this range of potential with bismuth reduction. In the reverse scan, only one dissolution peak (C) is observed at 0.009 V.vs.SCE it corresponds to the bismuth dissolution. No dissolution peak corresponding to manganese element is observed.

In the voltammogram with 1M of ammonium sulfate, the behaviour is almost the same except at -1.65 V.vs.SCE where a further increase in current density is observed, this is attributed to the discharge of both Mn^{2+} and Bi^{3+} and hydrogen reduction.

In the reverse scan, a dissolution peak (A) observed at -1.4V.vs.SCE is attributed to the Mn dissolution. This dissolution peak has a negative current density value because the cathodic reduction of H^+ and H_2O are still occurring there; this phenomenon was also observed by other authors [15]. Two other peaks are observed in this voltammogram, the first one at -0.5V.vs.SCE (B) can be attributed to dissolution of manganese oxides or hydroxide, and the second one at 0.01 V.vs.SCE (C) to the dissolution of Bi as previously reported in the first votammogram.

3.2 Morphological characterization

According the electrochemical study, thin films of Mn-Bi system have been electrodeposited on cooper substrate at different potential and during a deposition time of 300 s.

The SEM images of the deposit obtained at two different potential is showed in fig.4.

As we can see, the morphology of the deposit has an heterogeneous appearance, with a dispersed grains of bismuth (white area) and a more continuous manganese deposit (dark area), the appearance is related to the difference between the equilibrium potential of the two redox couple and to the strong immiscibility of the two elements.

The deposits realized at two different potentials is characterized by different grain size, this is attributed to the role of hydrogen evolution: the relatively low grain size may be induced by the comparatively large hydrogen evolution rate which is more important at -1.9 V.vs.SCE.

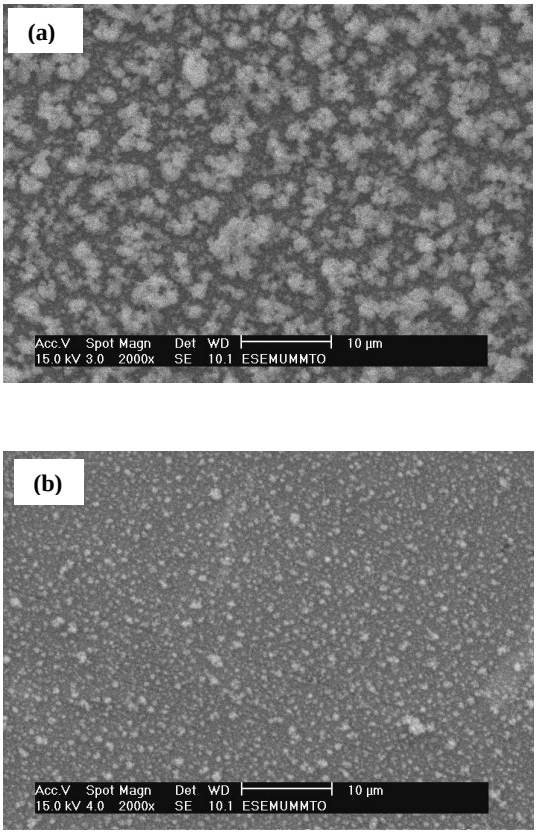

Figure 4.SEM images of the Mn-Bi electrodeposited on cooper substrate, (a) E= -1.8V.vs.SCE, (b) E= -1.9V.vs.SCE.

3.3 Physico-chemical characterization

The chemical composition of the deposits was estimated by energy dispersive spectroscopy (EDS).
EDS analysis showed that the deposits contain essentially manganese and bismuth with almost the same intensities. We note also the presence of oxygen in EDS spectrum, confirming the presence of Mn oxides, as observed in the electrochemical study; the cooper substrate peak was also detected indicating that the deposited film is thin.
The manganese and bismuth peak intensities obtained at E= -1.9 V.vs.SCE are lower than the ones obtained at E= -1.8 V.vs.SCE; this observation can be explained by the hydrogen ion reduction which decreases the deposit efficiency (Fig. 5).

4. Conclusions

In this study, Mn-Bi thin films were successfully electrodeposited on copper substrate from a mixed sulfate-nitrate bath.
According to the electrochemical study, the addition of ammonium sulfate in the electrolytic bath affects the electrodeposition kinetics of Mn, the presence of ammonium sulfate seems to be essential to grow manganese deposit with good coverage and relatively good efficiency.
The morphological characterization of the deposit by scanning electron microscopy shows a heterogeneous surface with a dispersed bismuth grains and a more continuous manganese deposit. This appearance is attributed to the difference between the equilibrium potential of the two redox couple and to the strong immiscibility of the two elements.
The EDS analysis indicate the presence of Mn and Bi peaks with almost the same intensities.
Annealing of the deposit is required to cause interdiffusion between the two species and to form a MnBi alloy.

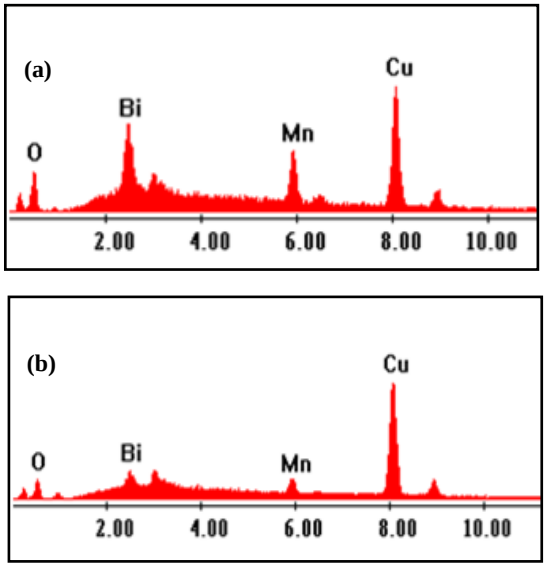

Figure 5. EDS spectrum of Mn-Bi thin films electrodeposited on cooper substrate, (a) E=1.8V.vs.SCE, (b) E=-1.9V.vs.SCE.

References

[1] Y.Dahmane, L.Cagnon, J.Voiron, S.Pairis, M.Bacia, L.Ortega, N.Benbrahim and A.Kadri, *Journal of Physics D: Applied Physics* 39 (2006) 4523–4528.
[2] E. Clifford, M.Venkatesan, J.M.D.Coey, *Journal of Magnetism and Magnetic Materials* 272-276 (2004) 1614-1615.
[3] Y. Liu, J. Zhang, Z. Ren , S. Cao , X. Zhang , G. Jia , X. Li , K. Deng, J. Zhang, *Current Applied Physics* 7 (2007) 555–560.
[4] K. Kang, A. R. Moodenbaugh, L. H. Lewis, *Applied Physics Letters* 90 (2007) 153112.
[5] K-U.Harder, D.Menzel, T.Widmer, J.Schoenes, *Journal of Applied Physics* 84 (1998) 3625-3629.
[6] U. Deffke, G.Ctistis, J.J.Paggel, P.Fumagalli, U.Bloeck, M.Giersig, *Journal of Applied Physics* 96 (2004) 3972-3975.
[7] Q.Fang, R.Fang, S.Zhang, D.Dai, *Journal of Applied Physics* 86 (1999) 3878-3880.
[8] S.Higashi, T.Ohshima, S.Mizuno, H.Tochihara, *Surface Science* 600 (2006) 591-597.
[9] P. Wei , O.E. Hileman Jr, M. Reza Bateni , X. Deng, A. Petric, *Surface & Coatings Technology* 201 (2007) 7739-7745.
[10] W. Li, S. Zhang, *Applied Surface Science* 257 (2011) 3275–3280.
[11] M. Yang, Z. Hu, *Journal of Electroanalytical Chemistry* 583 (2005) 46-55.
[12] B. Benfedda, N.Benbrahim, A.Kadri, E.Chainet, F.Charlot, S.Coindeau, *Electrochimica Acta* 56 (2011) 1275-1282.
[13] P. Díaz-Arista, G. Trejo, *Surface & Coatings Technology* 201 (2006) 3359–3367.
[14] J.Gong, G. Zangari, *Journal of The Electrochemical Society* 149 (2002) C209-C217.
[15] J. Wu, C.D. Johnson, Y. Jiang, R.S. Gemmen, X. Liu, *Electrochimica Acta* 54 (2008) 793–800.

Journal of New Technology and Materials
JNTM
Vol. 02, N°02 (2012) 22-24

OEB Univ. Publish. Co.

Measurement of skin temperature during dye laser treatment

J. Toumi[1], S. Tarabichi[2], A. Wabbi[3] and I. Assaad[4]
[1]*Higher Institute of Laser Research And Applications, Damascus University,. e-mail: johnny-toumi@hotmail.com*
[2]*Physics department, College of Science, Damascus University.*
[3]*Department of Physics, The Higher Institute of Applied Science and Technology, Damascus, Syria.*
[4]*HILRA, Damascus, Syria*

Received: 10 September 2012, revised: 17 November 2012, accepted: 17 November 2012

Abstract:
The aim of this study is to analyze thermal effects produced by laser stimulation during skin treatment. The focus of this paper is on experimental results for a new parameter, "active time" as recorded by an infrared camera during Dye Laser skin treatment of Syrian subjects with the varying skin tones representative of this population.
Index Terms: *Skin temperature, Temperature decay, Infrared camera, Pain threshold*

1. Introduction

The thermal study is one of the most important studies to determine the selection of laser parameters used in a specific thermal skin treatment. The thermal study records the relation between temperature rise and the intensity of the laser beam. The determination of the laser's wavelength is related to the specified treatment. In addition to the temperature variation study, other parameters should also be determined, such as pulse shape and duration. [1,2,3]
In our study, we focused on the use of 595 nm Dye Laser stimulation. This treatment is used for pigmented and vascular lesions, both of which are common in Syria. This paper is dedicated to the study of thermal temporal effects produced by using this laser on 12 different Syrian patients with the following conditions: pigmented lesion, port wine stain, spider hemangioma, telangiectasia, burn, and spider (varicose) veins.
Cooperating institutions were the Higher Institute of Laser Research and Applications and Hospital of Dermatology at Damascus University. We used a Fluke Ti55 thermal camera to capture thermal images and videos; we also used Matlab for analysing the pictures and videos used.
Several papers report on the thermal effects of laser irradiation on skin:
In 2006, M. Leandri et.al measured skin temperature of 8 subjects after Nd:YAP and CO_2 laser stimulation.
In 2010, Chunhui Li et. al studied thermal effects of laser ultrasonic on chicken skin using simulation and experiments.
In 2007, Wim Verkruysse et. al did temperature analysis for laser induced skin temperature to predict Individual Maximum Safe Radiant Exposure.

2. Theoretical Study

Before studying the thermal effect on skin, one must understand that the layers of the skin have different thermal parameters and thus have a different light-skin interaction.
Skin consists of two layers, the outer epidermis and the inner dermis. Under the dermis lies the subcutaneous layer. This layer, which is not part of the skin itself, is composed of proteins and adipose tissue. The epidermis consists of four to five layers. The total thickness of these layers is around (100 μm), 90% of epidermis is made of keratinocytes. The thickness of the dermis is approximately 1 mm. It is supplied with blood and nerves. Nearly 75% of dermis is made of two proteins, collagen and elastin, which provide the skin its strength and elasticity. [1]
When laser light falls on the skin, it takes several actions, the most important of which are absorption and scattering.
1- Absorption, described by absorption coefficient μa , is mainly caused by pigments, e.g. melanin, hemoglobin, protein and water. Light intensity decreases with the depth according to the Beer-Lambert law because of absorption. When skin absorbs the light, the skin temperature rises via energy fluency.
2- Scattering, described by scattering coefficient μS, occurs because of the volume, morphology and structure of atoms and molecules. Scattering is the main cause of the spread of the thermal spot induced by the laser when compared to laser's cross section. The effect of scattering is outside the scope of this paper. [5]

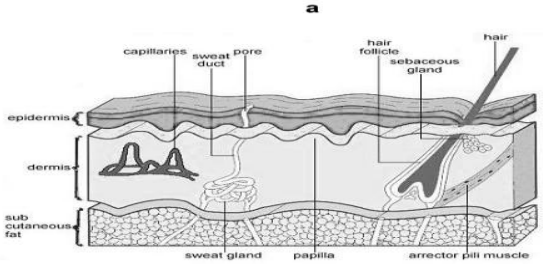

Figure 1. (a): Skin has a layered structure of epidermis and dermis. Many small structures are embedded in the dermis.

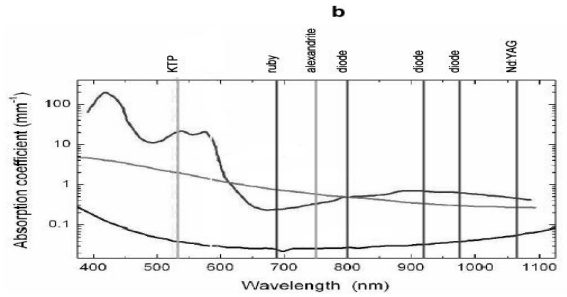

Figure 1. (b): Absorption spectra of the skin's main absorbers: water (blue), melanin (brown) and hemoglobin (red). The wavelengths of some important dermatological lasers are shown on the top of graph (b). [6]

3. Experimental work and results

3.1 Laser system and detectors

We used a Dye laser (595 nm) at the Hospital of Dermatology of Damascus University. The laser is capable of producing pulses between 0.5 ms and 40 ms. Flounce measurements were performed using the integrated power-meter within the laser system.
A thermal imager (type Fluke Ti55) is used to obtain thermal images. This imager has the following specifications:
Resolution: 320 x 240 pixels.
Max frame rate: 60 fps.
Spectral band: 8 μm to 14 μm.
Focusing: Single finger manual focus.
The following values were set for these parameters:
Grayscale Picture mode.
Minimum and maximum temperature scale and fixed optimized values depending on each subject's case.
Emissivity at 0.98.
Frame rate mode: NTSC (29.97). This frame rate is the maximum value we can get and record on a PC from this camera.
We took the thermal images sequence in the form of video capture.

3.2 Results and discussion

We used Matlab 2011a as platform for the analysis of the thermal video data.
The measurements were taken for several native Syrian subjects with different sex, age and skin tones. The laser parameters were identical across subjects: fluency was 7.1 J, pulse duration was 0.5 ms, and the laser cross section's diameter was 7 mm.
We introduced a new value ("active time") to determine the temporal measurement of the thermal effect. This parameter (time) was taken by determining the width of temporal temperature curve (stimulated by the laser pulse) at the damage threshold temperature. This value is called "active time".
Considering that active time is essential when using thermal cameras with a slow frame rate compared to laser pulse duration, one cannot trust the camera to record the exact maximum temperature on skin. Such a temperatures is reached extremely quickly after laser stimulation, therefore any measurement related to this value (like taking relaxation time at 50% or ~30% of the max temperature rise) is likely to be inaccurate. In addition, taking active time means taking the portion of time when the temperature damages the skin (i.e when it hurts the patient). We considered the damage temperature to be at 41o C based on discussion in [6].
The results were taken both with and without air cooling as shown in the next tables:

Skin Tone	Active time (s)
2	2.15
2-3	1.15
3	0.042
4	0.04

Table 1. Active time for different subjects with cooling.

Skin Tone	Active time (s)
2	6.5
2-3	6
3	5.6
4	5.2

Table 2. Active time for different subjects without cooling.

As the above results show, cooling methods can decrease active time from about 3 to 70 times depending on skin tone. The influence of cooling time was greater for darker skins.
For skin tone itself in both cases with and without cooling, we notice that active time decreases when skin tone increases. For the same skin tone, active time decreases when cooling is present.
Our results are consistent with the references (2,3) that dealt with relaxation time and its variation with skin tone and cooling, note that we have adopted the active time which is calculated according to a fixed criteria: the damage threshold temperature of human skin, where the limits of this threshold is fixed whatever the maximum energy, unlike the relaxation time. Relaxation time and active time vary according to the applied energy, but the threshold temperature at which the relaxation time is calculated depends on the maximum energy, on the other hand the threshold temperature at which active time is calculated is fixed. The effect of energy, skin tone and cooling play the role in the time required for this threshold.

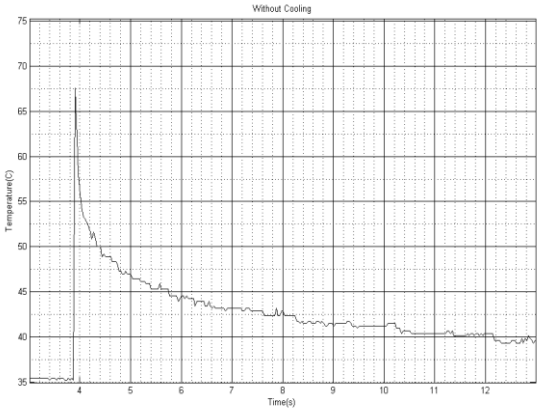

Figure 2. Skin temperature vs. time after laser stimulation for a subject with skin tone 4 and without cooling.

4. Conclusions

As our results show, a change in skin tone (within the range of typical Syrian subjects) leads to vast variation in active time calculated at the threshold of 41o C. The presence of cooling makes these changes more dramatic. Doctors should keep the changes in active time and values in mind while treating a subject with a laser or when designing a laser system for skin treatment which is optimized for lighter or darker skin tones.

References

[1] Wim Verkruysse, Wangcun Jia, Walfre Franco, Thomas E. Milner and J. Stuart Nelson," Infrared Measurement of Human Skin Temperature to Predict the Individual Maximum Safe Radiant Exposure (IMSRE)", *Laser in Surgery and Medicine* 39:757-766 (2007).

[2] Chunhui Li, Sinaan Li, Zhihong Huang, Wenbin Xu., ''Skin Thermal Effect by FE Simulation and Experiment of Laser Ultrasonic," *Applied Mechanics and Material*, Vols. 24-25, (2010) pp 281-286.

[3] M. Leandri, M. Saturno, L. Spadavecchia, G.D. Iannetti, G. Cruccu, A. Truini, ''Measurement of skin temperature after infrared laser stimulation,''. *Elsevier, neurophysiologie Clinique,* 36 (2006) 207-218.

[4] Mrtin Gorjan, "modeling and measurements of laser-skin thermal interaction" (graduate seminar) (2008).

[5] Jorgen Serup and G. B. E. Jemec, Handbook of Non-Invisive Methods and the Skin. (1) (1995).

[6] Tuan Vo-Dinh, Biomedical photonics handbook (r857.06 b573 2002).

Journal of New Technology and Materials
JNTM
Vol. 02, N°02 (2012) 25-28

OEB Univ. Publish. Co.

Humidity Sensing and Electrical Properties of HMDSO Plasma Thin Film

N. Guermat[a,b], A. Bellel[b], S. Sahli[c], Y. Segui[d] and P. Raynaud[d]

[a]*Département d'Electronique, Faculté de Technologie, Université de M'sila, BP.166, Route Ichebilia, M'sila 28000 Algerie, e-mail: g_noubeil@yahoo.fr*

[b]*Laboratoire des Etudes de Matériaux d'Electronique pour Applications Médicales (LEMEAMED), Faculté des Sciences de l'Ingénieur, Université Mentouri de Constantine 25000*

[c]*Laboratoire de Microsystèmes et Instrumentation (LMI), Faculté des Science de l'Ingénieur, Université Mentouri de Constantine 25000*

[d]*Laboratoire Plasma et Conversion d'Energie (LAPLACE), Université Paul Sabatier, 118 route de Narbonne-31062 Toulouse – France*

Received: 04 March 2012, revised: 14 November 2012, accepted: 24 November 2012

Abstract

This paper reports the study of humidity-sensitive and electrical properties plasma polymerization of hexamethyldisiloxane (pp-HMDSO) thin film based sensors. The humidity sensitive film was deposited by glow discharge at low frequency power (19 KHz) in a capacitively coupled parallel plate plasma reactor. The sensor design comprises the intredigited electrodes and the absorbing layer. The sensor was calibrated in terms of impedance as a function of relative humidity, using a Frequency Response Analyzer. The signal frequency range was between 10^2 to 10^7 Hz with amplitude of 3V. Structural analysis of the sensitive layer was carried out by Fourier Transform Infrared spectroscopy (FTIR). Electrical properties, including capacity-humidity, hysteresis of the elaborated sensor were investigated. Interdigital electrodes and sensing layer were modeled using equivalent circuits to resolve the effects of adsorption and ion migration. The HMDSO films showed promising characteristics for humidity sensor development.

Keywords: *HMDSO; Humidity sensor; Hysteresis; Impedance analysis.*

1. Introduction

A humidity sensor is a device which can covert the ambient moisture variation into an electrical signal (resistance or capacitance) variation, so it can be easily installed in electronic equipment to detect or control the ambient humidity. The humidity sensors based on polymers can be classified as resistive-type and capacitive-type [1] sensors. They have simple fabrication and small hysteresis. The sensing mechanism of these materials is that the adsorption of the surrounding water vapor enhances the surface ionic conductivity of sensing materials. In this paper, we report the humidity sensing properties of pp-HMDSO thin film elaborated by low frequency plasma discharge (19 KHz).

1. Results

1.1 Humidity sensing properties

The plasma polymerized HMDSO thin films deposited on two-intredigitated aluminum electrodes were used as sensor element and evaluated for humidity detection under an applied voltage of 3V and signal frequency of 1 kHz. The measured result was achieved by HP 4280A-model LCZ meter. Fig. 1 shows the measured impedance responses over thin pp-HMDSO film in the range of relative humidity (RH) of 10 to 95% at temperature of about 27 °C.

The impedance of the sensor decreased two orders of magnitude when relative humidity decreased from 30% to 95% on a semi-logarithmic scale. Between 10 and 30 % of RH, the deposited films were found to be insensitive to water vapor. The pp-HMDSO film sensor did not show a visible change of the electrical impedance, the value of this later was in order of about 10^6 Ω. Increasing RH beyond 30% gives rise to an abrupt impedance decrease. The value of the electrical impedance decrease significantly until reaching the value of 10^4 Ω. At lower RH, the electrical response is caused by proton hopping between chemisorbed hydroxyl groups. Afterwards, when the amount of physisorbed water molecules starts to increase, the hydronyum ion, H_3O^+, is most likely the charge carrier. Furthermore, pp-HMDSO based sensor showed small hysteresis (2%), excellent sensitivity to humidity and wide scale of impedance (Fig.1), which indicated that the reversible absoption/desorption is easily achieved in this case [2]. The capacitance of the sensor increases with RH increasing, it changes a little at low RH, and changes greatly at high RH (Fig.5). The Fig. 2 shows different relationship curves between impedance and relative humidity for different frequencies. The impedance of the sensor depends on frequency at low humidity and it is independent at high humidity. The response sensitivity of sensor decreases significantly at high frequencies.

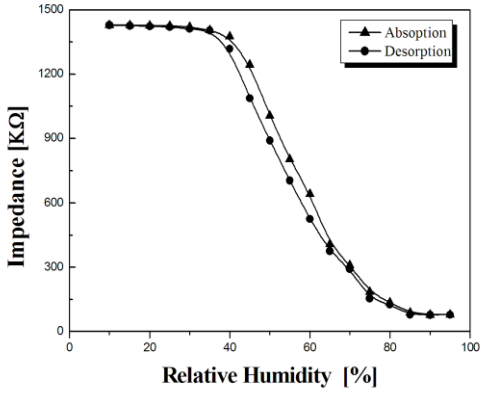

Figure.1. Humidity–impedance characteristics of pp-HMDSO based sensor.

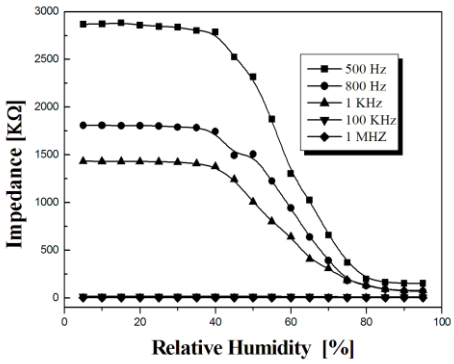

Figure.2. The absorption humidity curves at different frequencies.

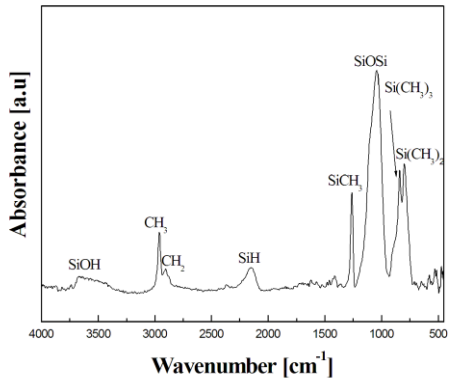

Figure. 3. Typical FTIR absorption spectrum of pp-TEOS film.

1.2 Structural properties

FTIR analysis was carried out in absorption mode to study the chemical composition of the deposited thin films. The resulting spectrum is shown in Fig.3 which revealed several peaks assigned to different chemical groups listed in the Table 1. The spectrum of the plasma polymer deposited at 8 W with thickness of about 250 nm from pure HMDSO reveals strong peaks at around 800, 840 and 1049 cm^{-1} corresponding respectively to Si-$(CH_3)_2$, Si-$(CH_3)_3$ and Si-O-Si groups. Another peak which is representative of the organic groups (Si-CH_3) appears at 1261cm^{-1}. The sensitivity to humidity is highly affected by the presence of the organic groups (Si-CH_3). In addition, FTIR spectrum shows also a peak with low intensity at around 3669 cm-1 attributed to the stretching mode of surface silanols (Si-OH), which can provides hydrophilic capability for water absorption through a hydrogen-bonding force.

Table 1.
Absorption peaks range and their assignments

100% HMDSO Wavernumner [cm^{-1}]	Group [3-4]
800	Si-$(CH_3)_2$
840	Si-$(CH_3)_3$
1049	Si-O-Si
1261	Si-CH_3
1410	Si-CH_3
2146	Si-H
2902	CH_2
2967	CH_3
3669	Si-OH

1.3 Complex impedance

Impedance spectroscopy is a powerful technique to understand the conduction mechanisms of humidity sensors. Therefore, the impedance plot was adopted to elucidate the transport process by ions in the conduction mechanism of the pp-HMDSO films. Complex impedance plotting techniques can help in building the equivalent circuit model and then analyzes the mechanism of the humidity sensing material. It is known that a semicircle in an impedance spectroscopy plot represents a resistor R in parallel with a capacitor C. The angular frequency of the peak of the semicircle ω_p is such that $\omega pRC = 1$. The value of the resistor and capacitor with the frequency determine whether semicircle is closed or not. The impedance measurements were carried out in the frequency range of 300 Hz to 800 kHz at humidities of 10 to 95%RH, an ac voltage of 3V. The typical complex impedance spectra (Nyquist plots) of the pp-HMDSO film at different humidities are shown in Fig. 4. The electrode geometry and thickness were constant for all measurements; the only variable parameter in our measurements was the frequency signal. Zre and Zim are the real and imaginary parts of the complex impedance, respectively. It was observed that at low humidity levels, the Nyquist plot describes an arc with a very large curvature and the semicircle is not closed. This radius decreases with increasing RH due to the effect of the physisorbed water layer on sensor surface [5]. The decrease in the impedance is due to the increase in electrical conductivity by H_3O^+ and H^+ ions in the dielectric film. From the Nyquist plot, it can be understood that the sensor contains a parallel combination of R and C. It is seen that at low frequency,

impedance is purely resistive and at high frequency it is purely capacitive in nature. At low humidity, the resistance is very high then decreases when the RH increases and becomes comparable to capacitive reactance [5]. In other words, at low RH (<40% RH), only a small amount of water is absorbed, and the response of the sensor resistance to RH was mostly caused by the structure change in the film [6]. When RH increased (50% RH), the inclined semicircle appeared. Many authors [5-8] have explained that it is due to a kind of polarization and it can be modeled by an equivalent circuit of parallel resistor and capacitor which agree with the result of Fig. 5.

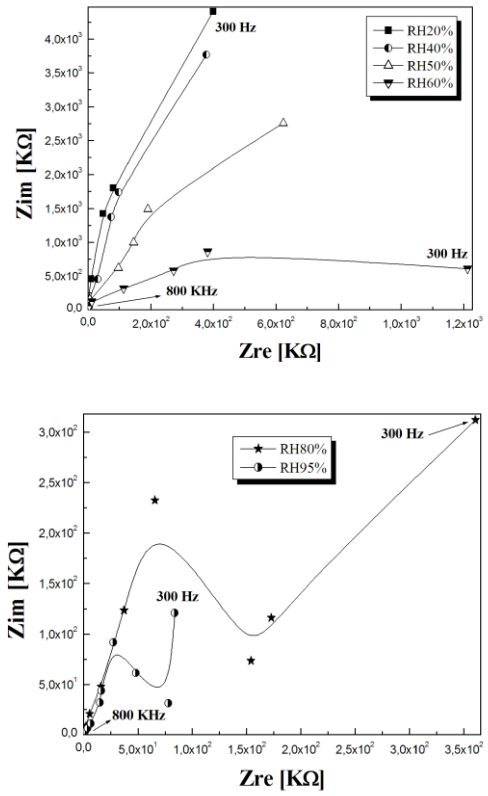

Figure 4. The complex impedance plots of

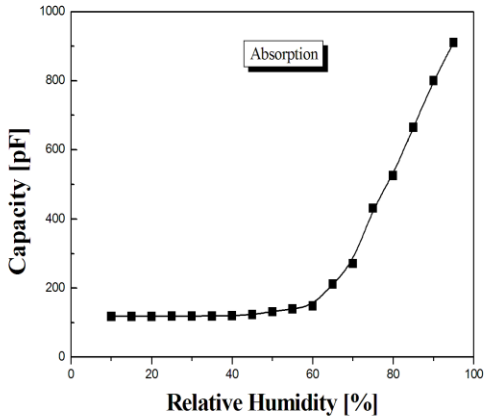

Figure 5. The relationship curve between capacitance and relative humidity.

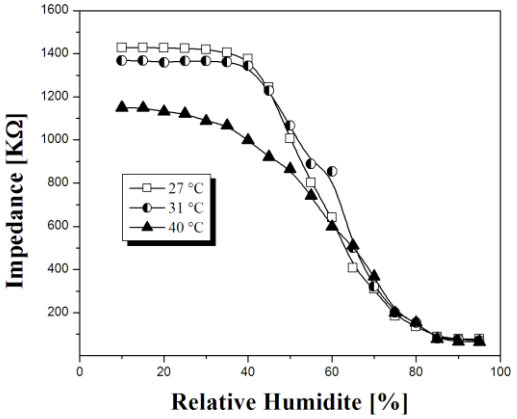

Figure 6. Impedance vs. relative humidity for the pp-HMDSO film at various temperatures.

1.4 Temperature property

Fig. 6 gives the curves of the impedance versus RH for different temperatures at frequency of 1 KHz. It is noticed that as the temperature increases, the impedance of the sensor decreases. In general, the ion transport in pp-HMDSO is strongly dependent upon the operating temperature. At higher temperature, the impedance was decreased because of the improved movement of the carrier ion. Therefore, the compensation of temperature is necessary for the application to a humidity sensor. The thermal movement of molecule is an internal cause for the material polarization. And the electric field determines the direction of the polarization. As the temperature rises, the thermal movement of molecule becomes strong, and the increase of the polarization results in the decrease of the impedance value.

2. Conclusions

The humidity sensor based on pp-HMDSO thin film exhibited good electrical response to relative humidities from the range of 10 to 95% of RH with small hysteresis of about 2%. The Cole-Cole plots of the complex impedance of the HMDSO layer in different relative humidity show a tendency that the shapes of the curves change from a semicircle to a line with the increasing of RH. An analysis of an equivalent circuit of parallel resistor and capacitor and the complex impedance leads us to the following explanation: at low frequency the impedance is purely resistive and for high frequency it is purely capacitive in nature.

Acknowledgment

This work was supported by the Algerian-French cooperation.

References

[1] T. Zhang, X. Tian, B. Xu, W. Dong, L. Sun, S. Xiang, D. Gao, *Journal of Materials Science Letters*, 19 (2000) 1419 – 142.

[2] N. Guermat, A. Bellel, S. Sahli, Y. Segui, P. Raynaud, *Thin Solid Films*, 517 (2009) 4455–4460.

[3] A. J. Choudhury, J. Chutia, H. Kakati, S. A. Barve, A. R. Pal, N. S. Sarma, D. Chowdhury, D. S. Patil, *Vacuum*, 84 (2010) 1327-1333.

[4] G. Sun, G. Grundmeier, *Thin Solid Films*, 515 (2006) 1266–1274.

[5] K. P. Biju, M. K. Jain, *Thin Solid Films*, 516 (2008) 2175–2180.

[6] P. G. Su, W.Y. Tsai, *Sensors and* Actuators, B 100 (2004) 417–422.

[7] C. P. L. Rubinger, C. R. Martins, M.-A. De Paoli, R.M. Rubinger, *Sensors and Actuators, B* 123 (2007) 42–49.

[8] J. Wang, B. K. Xu, S. P. Ruan, S. P. Wang, *Materials Chemistry and Physics*, 78 (2003) 746–750.

Journal of New Technology and Materials
JNTM
Vol. 02, N°02 (2012) 29-33

OEB Univ. Publish. Co.

Extraction of important parameters of a silicon diode used as particles detector

A. Saadoune, L. Dehimi, N. Sengouga, W. Terghini and M.L. Megherbi
Laboratory of Metallic and Semi- conducting Materials, B.P. 145, University of Biskra, Biskra, 07000, Algeria,
Corresponding author: saadounea@yahoo.fr

Received: 1 May 2012, revised: 06 December 2012, accepted: 13 December 2012

Abstract:

The Capacitance-Voltage characteristics (C-V) and the resistivity (ρ) of a p^+nn^+ silicon diode used as a particle detector is numerically simulated using the finite difference method. These characteristics permit to extract the important and useful parameters for the design of a detector diode used in a harsh environment and subjected to strong fluencies, such as the depletion voltage (V_{dep}), the effective concentration and the maximum resistivity, the reduction rate of the donors (c) and the introduction rate of defects (g). When this junction is subjected to strong radiations, physical defects which are created in the semiconductor lattice have undesirable effects and can degrade the performance of the detectors. These defects behave like deep levels and/or generation recombination (g-r) centres.
The depletion voltage and the effective concentration were calculated by using C-V characteristic. The evolution of the effective density in function with the density of traps acceptor led as to find the redaction rate of the donors (c) and the introduction rate (β).
The resistivity increases with increasing of the deep acceptor density to achieve the intrinsic resistivity (maximum).
Keywords: Semi-insulating; Semiconductor; Diode; Radiation damage; Modeling.

1. Introduction

Many poorly conducting semi-conducting and semi-insulating electronic materials show unusual electrical properties such as non-Ohmic behaviour. These experimental findings are often tacitly ascribed to their highly impure state with many defects and impurities but not analysed in detail [1, 2].
Most previous calculations have been carried out mainly as a demonstration of the relaxation theory [3-5]. The present work is designed as a practical and helpful analysis to enable the experimenter to understand the internal state of his sample and what its likely impurity content is. Here we describe the main features which are observed experimentally in order to extract the important and useful parameters, using a typical diode structure as an example, to explain the physical processes occurring and discuss the implications and applications. The aim is to explain the physical reasons underlying the experimental results and the effects of different types of defects. By making this range of generic calculations with different parameters we have established that the results obtained are robust and insensitive to the details of the sample such as the type and magnitude of the trap energy levels so that general categories such as deep or less-deep levels can be considered. These results are as expected for low g-r centre density. The variation with trap concentration or cross-section can be deduced from the analytical calculation. This should enable some general idea to be obtained about the dominant defect and how its properties may perhaps be modified by additional doping.

Defects can be introduced into a perfect semiconductor crystal lattice by chemical doping or by the displacement of atoms by irradiation. The electrical properties are changed and the effect can be categorized by two basic mechanisms, the introduction of mid gap energy levels which act as generation-recombination (g-r) centres and the introduction of other energy levels within the energy gap. In this analysis we will simplify the many variables by assuming that the g-r centres generate or recombine electron hole pairs and are, on average, electrically neutral. The other centres can be neutral or charged (ionized) depending on the position of the Fermi level. For convenience we introduce the terminology of Deep Acceptors (DA) which is further from their band edge than mid-gap and Less Deep Acceptors (LDA) which are closer to their band edge, but are not permanently ionized.

2. This work

The modeling was carried out using the package KURATA [6]. The PIN diode is a $P^+N^-N^+$ structure with a long N^- or intrinsic layer. The structure is divided into M points along the x-axis. A higher density of points was used near the metallurgical junctions. The program uses an explicit integration method to solve the one dimensional Poisson, current density and continuity equations for electrons and for holes using full Shockley-Read-Hall statistics. The variables computed are the electron density (n), the hole density (p) and the potential (V) at each mesh point of the structure. The initial values of n and p are simply the corresponding doping densities. That is, in the p-region $p = N_A$ and $n = n_i^2/N_A$ while in the n-region $n = N_D$ and $p = n_i^2/N_D$.

The boundary conditions are as follows; at the far end of the P^+ contact $p = N_A$, $n = n_i^2/N_A$ and $V = 0$ (the reference voltage) while at the far end of the N^+ contact $n = N_D$, $p = n_i^2/N_D$ and V = the applied voltage. Here, N_A and N_D are the acceptor and donor densities and n_i is the intrinsic carrier density.

The resistivity and the capacitance can be computed once n, p and V are known. These characteristics permit to extract the important parameters. The analysis was carried out for a silicon $P^+N^-N^+$ structure with $1x10^{11}$ cm^{-3} shallow donors (N^-). The contacts are P^+ ($N_A=10^{15}$ cm^{-3}) between 0 and 30 µm and N^+ ($N_D=10^{15}$ cm^{-3}) between 320 and 350 µm.

The sample is long in the sense that the excess charge distribution is mostly in short lengths near the ends. The contacts are made deep so that there is no significant depletion at x = 0 µm and at x = 350 µm. We assume sharp metallurgical junctions, mainly because we have established that the more realistic graded junctions make little difference to the results since the junction region itself is mainly depleted. This means that the details of the contact do not matter much. The temperature was assumed to be 300K.

The intrinsic carrier concentration at room temperature is $n_i=1.45x10^{10}cm^{-3}$ while the dielectric relaxation time is $\tau_D \sim 10^{-9}$s. These simulation results are as expected for low g-r centre density N_{g-r} and we will take 10^{10} cm^{-3} using $\tau^{-1}=\sigma v_{th} N_{g-r}$, where v_{th} is the thermal velocity of carriers. A typical value of 10^{-13} cm^2 is used for the cross-section, σ [7, 8] and the centers are at mid-gap. Conventionally the capacitance of a semiconductor diode has often been theoretically defined from the change in the space charge density by the applied bias voltage. In our case the internal charge distribution is complex with static and mobile charges and there are redistributions internally so that this simple approach to the calculation is inappropriate. Here we use another definition of the capacitance of a diode based on the energy capacitance C_W [9, 10] which is defined by:

$$C_W = \frac{1}{|\psi|}\frac{dW}{d\psi} \tag{1}$$

ψ is the voltage difference defined by:

$$\psi = V_{bi} - V_A$$

Where V_A is the applied voltage, V_{bi} is the built-in voltage of the diode and W is the electrostatic energy calculated from the electric field distribution $E(x)$ as:

$$W = \frac{\varepsilon.\varepsilon_0}{2}\int_0^l E(x)^2\,dx \tag{2}$$

ε_0, permittivity in vacuum, ε, relative permittivity and l length of the structure.

The electrical resistivity of a structure (based on a semiconductor) is directly related to the densities of electrons and holes.

$$\rho = \frac{1}{q(\mu_n n(x) + \mu_p p(x))} \tag{3}$$

Where:

$$\rho_{max} = \frac{1}{2q\sqrt{\mu_n.\mu_p}.n_i} \tag{4}$$

3. Results

The calculations demonstrate various effects which may be observed in real samples. These represent simple special cases because there are too many variables for a wider investigation. The aim of these calculations is to show that care must be taken in the use of V_{dep} to obtain N_{eff} and the interpretation of the value obtained. Any conclusions drawn from the results obtained must be emphasized to be approximate.

$$V_{dep} = \frac{w^2 q|N_{eff}|}{2\varepsilon\varepsilon_0} - V_{bi} \tag{5}$$

The depletion voltage (V_{dep}) is extracted using the CV characteristics. Thus depletion voltage is given by intersect of the straight line with linear voltage dependence below depletion and saturated, constant line above depletion as shown in figure 1 [11].

Irradiation of a PIN diode with the starting intrinsic material lightly n-type, with no known traps, is found experimentally to produce an initial reduction of N_{eff} and then an increase roughly proportional to the fluence [12-15]. It is assumed that the radiation damage produces both g-r centers and shallow acceptors which compensate the shallow donor doping. The material changes type and the depletion junction moves to the other end of the intrinsic layer. This is probably a correct assumption and the type inversion occurs when the new shallow acceptor concentration becomes greater than the original donor concentration.

Consider the results of Figure2 for 10^{11} cm^{-3} shallow donors doping. For a less deep acceptor at 0.30eV above the valence band, type inversion occurs at an acceptor density of 9×10^{10} cm^{-3} as the 10^{11} cm^{-3} shallow donors doping are compensated. However, for the same conditions in the case of deep acceptors at 0.70eV, type inversion occurs at an acceptor density of about 5×10^{13} cm^{-3} (Fig.2).

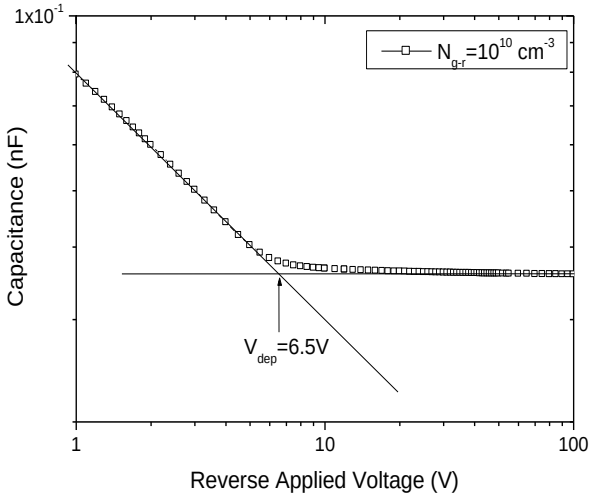

Figure1. C-V characteristics in log-log scale of a semiconductor $P^+N^-N^+$ diode ($N_D=10^{11}$ cm^{-3}) with g-r centre density of 10^{10} cm^{-3} and in the absence of traps [11].

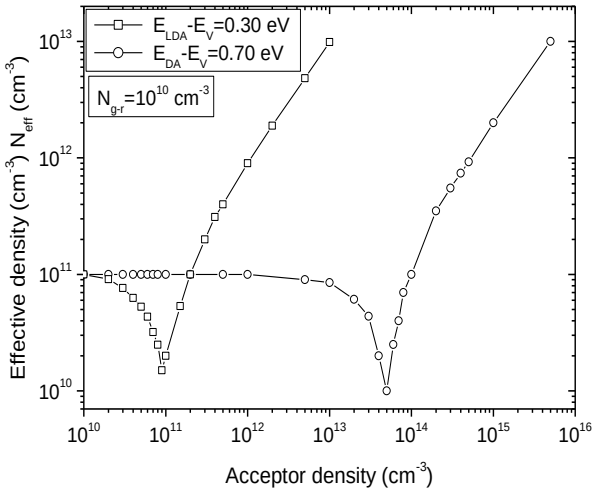

Figure 2. The effective density (N_{eff}) is shown in the presence of a less deep acceptor at 0.30 eV and a deep acceptor at 0.70 eV with an increasing density with *g-r* centre density of 10^{10} cm^{-3}.

This occurs because the deep acceptors are located in the tail of the Fermi-Dirac distribution and not fully ionized when the Fermi level is near mid-gap. Thus, an independent knowledge of the energy of the traps introduced by the irradiation is needed in order to obtain a correct value for the effective density.

Many workers have experimentally found that N_{eff} changes as a function of the fluence, φ. The N_{eff} behavior of n-type silicon can be fitted to the empirical function [16].

$$N_{eff} = N_A - N_D \exp(-c\Phi) + B\Phi \quad (6)$$

Where N_D is the initial donor concentration, N_A is the initial acceptor concentration (the compensation level), c describes the redaction rate of the donors and β is the parameter accounting for the introduction rate of acceptor-like defects. The radiation induced acceptor defects are found to be dominant: it has actually been measured that the doping concentration of initial n-type silicon diodes decreases progressively as a function of the received fluence until the diodes invert to effectively p-type. After conductivity type inversion, the p-type N_{eff} increases linearly with fluence. The parameterization of the radiation induced behaviour of n-type silicon diodes implies redaction rate of the donors and linear introduction rate of acceptor-like defects. Figure 3 and 4 shows an example of $Neff(V_{dep})$ versus acceptor density with fitting results according to Equation 6.

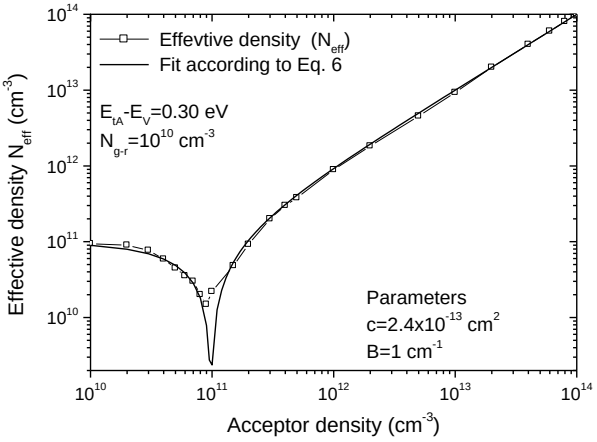

Figure 3. Evolution of effective density N_{eff} (V_{dep}) versus the density of less deep acceptor in the presence of low density of *g-r* with energy level of less deep acceptor.

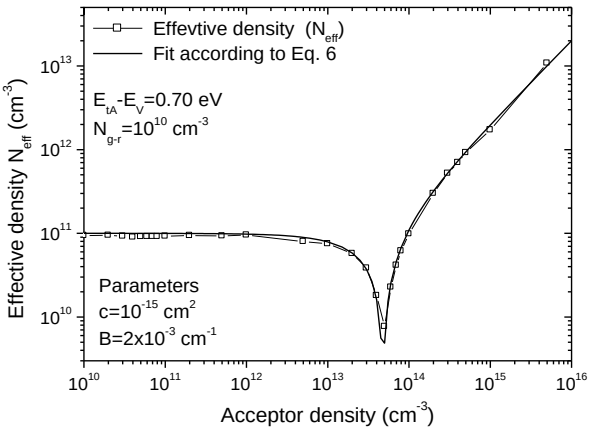

Figure 4. Evolution of effective density N_{eff} (V_{dep}) versus the density of deep acceptor in the presence of low density of *g-r* with energy level of deep acceptor.

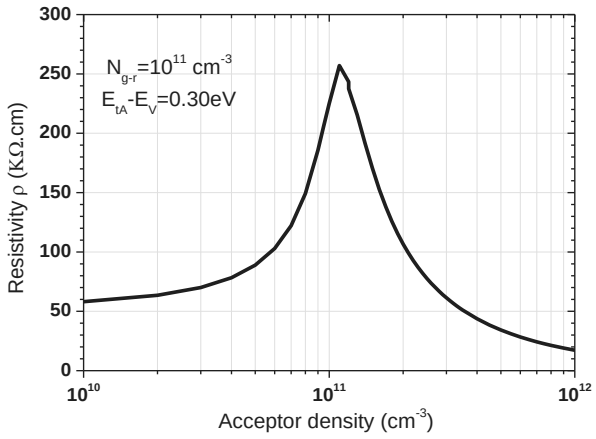

Figure 5. Resistivity as a function of density of less deep acceptor in the presence of low density of g-r with energy level of less deep acceptor.

After inversion, a simple model describes the silicon detector as a p-type diode, which junction develops from the n+ rear layer. However, this model is inadequate to describe some behavior of inverted detectors.

Figure 5 shows resistivity as a function of density of less deep acceptor in the presence of low density of *g-r*.

The resistivity increases as expected until acceptor density correspond the type inversion, but for further density of deep (less deep) acceptor decreases with a slower rate than the *Neff* increase as experimentally found, that the resistivity increases initially and then decreases with increasing fluence [17-19].

This indicates that a parameter associated to the material in thermal equilibrium (ρ) and a parameter correlated to the material under reverse bias condition (depletion regime) cannot be correlated as expected from the theory of non-irradiated semiconductors.

The resistivity is maximum (Figure 5) when the trap accepter ionized exactly compensates the shallow donor.

4.Conclusion

The study presented in this work is the extraction of important parameters for the design of the silicon diode $P^+N^-N^+$ used as particles detector, such as the depletion voltage (V_{dep}), the effective concentration and the maximum resistivity, the reduction rate of the donors (c) and the introduction rate of defects (β). An example of this is the radiation damage of silicon diodes. In this work radiation defects which are created are simulated as less and deep acceptors and generation-recombination (g-r) centers.

Results of this modeling show a change in the voltage needed for total depletion (V_{dep}). The other parameter affected is the effective concentration which shows the reversal of semiconductor type if the traps created are acceptors. These two parameters were calculated using the CV characteristic. The evolution of the effective density as a function of the density of acceptor trap led us to extract the reduction rate of the donors (c) and the introduction rate of defects (β).

The resistivity increases with increasing the density of acceptor trap this is due to the compensation of shallow donor doping by acceptors traps. It reaches a maximum value when total compensation is satisfied. After the compensation is satisfied the resistivity starts decreased with increasing the density of acceptor trap. This decrease indicates that the material is change the type.

The numerical simulation results obtained are leading to explain the phenomena observed experimentally and thus indicating the elements influencing the different characteristics. This led to the design of detectors more radiation hard.

References

[1] Dehimi L, Sengouga N, Jones BK., "Modelling of semi-conductor diodes made of high defect concentration, irradiated, high resistivity and semi-insulating material: the current–voltage characteristics," *Nucl Instrum Meth Phys Res.*, Vol. 519, No. 3, pp. 532–544, 2004.

[2] Dehimi L, Sengouga N, Jones BK., "Modelling of semi-conductor diodes made of high defect concentration, irradiated, high resistivity and semi-insulating material: the internal field," *Nucl Instrum. Meth phys Res., Vol.* 517, No. 1-3, pp 109-120, 2004.

[3] Van Roosbroeck W., "Current carrier transport with space charge in semiconductors," *Physical Review*, Vol. 123, No. 15, pp. 474-490, 1961.

[4] Qeisser H.J, "Semiconductors in the relaxation regime, Solid State Devices," *IOP Conf Ser.*, No. 15, pp.145-168. 1973.

[5] Haegel N.M., "Relaxation Semiconductors: In Theory and in Practice," *Applied Physics*, Vol. 53, No 1, pp.1-7, 1991.

[6] Kurata M., "Numerical analysis for semiconductor devices," Lexington (MA), Lexington Books, 1982.

[7] Karel O, Gobling C, Klinenberg R, Wunstorf R., "Electric fields in irradiated silicon pad detectors. Radiation Hard Semiconductor Devices for Very High Luminosity Colliders for Very High Luminosity Colliders," In: 4th RD50 Workshop, CERN, Geneva, 2004.

[8] McPherson M., "Emission and capture processes in radiation-damaged silicon semiconductor diodes," *Current Applied Physics*, Vol. 2, No 5, pp.359-364, 2002.

[9] Ogawa M., Matsubayashi H., Ohta H. and .all., "Accurate parameter extraction of heterojunctions based on inverse C-V simulation," *solid-state Electronics,* Vol. 38, No. 6, pp.1197- 1207, 1995.

[10] Saadoune A, Dehimi L, Sengouga N, McPherson N, Jones B.K., "Modelling of semiconductor diodes made of high defect concentration, irradiated, high resistivity and semi- insulating material: The capacitance–voltage characteristics," *Solid State Electronics*, Vol. 50, No. 7, pp.1178-1182, 2006.

[11] Saadoune A., "Paramétrisation des propriétés électriques d'une diode au silicium soumise à des hautes fluences de particules," Thèse de Doctorat, Université de Biskra, 2009.

[12] McPherson M., "Irradiated silicon detectors as relaxation devices," PhD Thesis, Lancaster University, 1998.

[13] Petasecca M, Moscatelli F, Passeri D, and Pignatel G U., "Numerical simulation of radiation damage effects in p- type and n-type fz silicon detectors," *IEEE Transactions On Nuclear Science*, Vol. 53, No. 5, pp. 2971–2976, 2006.

[14] Mara Bruzzi, "Radiation Damage in Silicon Detectors for High-Energy Physics Experiments," *IEEE Transactions On Nuclear Science*, Vol. 48, No. 4, pp. 960-971, 2001.

[15] Lazanua S, Lazanu I., "Correlation between radiation processes in silicon and long-time degradation of detectors for high- energy physics experiments," *Nuclear Instruments and Methods in Physics Research*, Vol. 580, No. 1, pp. 46-49, 2007.

[16] Fretwurst E., Claussen N., Croitoru N., Lindström G., Papendick B., Pein U., Schatz H., Schulz T., Wunstorf R., "Radiation hardness of silicon detectors for future colliders," *Nuclear Instruments and Methods in Physics Research*, Vol. 326, No. 1-2, pp. 357-364, 1993.

[17] Biggeri U, Borchi E, Bruzzia M, Lazanub S, Li Z., "CV and Hall effect analysis on neutron irradiated silicon detectors," *Nuclear Instruments and Methods in Physics Research,* Vol. 388, No. 3, pp. 330-334, 1997.

[18] Pirollo S., Biggeri U., Borchi E., Bruzzi M., Catacchini E., Lazanu S., Li Z., Sciortino S., "Radiation damage on p-type silicon detectors," *Nuclear Instruments and Methods in Physics Research,* Vol. 426, No. 1, pp. 126-130, 1999.

[19] Biggeri U., Borchi E., Bruzzi M., Lazanu S., "Hall effect analysison neutron irradiated high resistivity silicon," *Nuclear Instruments and Methods in Physics Research,* Vol. 360, No. 1-2, pp. 131-133, 1995.